

XMM-NEWTON AND CHANDRA OBSERVATIONS OF ABELL 2626:  
INTERACTING RADIO JETS AND COOLING CORE WITH JET PRECESSION?

KA-WAH WONG<sup>1</sup>, CRAIG L. SARAZIN<sup>1</sup>, ELIZABETH L. BLANTON<sup>2</sup>, AND THOMAS H. REIPRICH<sup>3</sup>  
*Astrophysical Journal, accepted*

ABSTRACT

We present a detailed analysis of the *XMM-Newton* and *Chandra* observations of Abell 2626 focused on the X-ray and radio interactions. Within the region of the radio mini-halo ( $\sim 70$  kpc), there are substructures which are probably produced by the central radio source and the cooling core. We find that there is no obvious correlation between the radio bars and the X-ray image. The morphology of Abell 2626 is more complex than that of the standard X-ray radio bubbles seen in other cool core clusters. Thus, Abell 2626 provides a challenge to models for the cooling flow – radio source interaction. We identified two soft X-ray (0.3–2 keV) peaks with the two central cD nuclei; one of them has an associated hard X-ray (2–10 keV) point source. We suggest that the two symmetric radio bars can be explained by two precessing jets ejected from an AGN. Beyond the central regions, we find two extended X-ray sources to the southwest and northeast of the cluster center which are apparently associated with merging subclusters. The main Abell 2626 cluster and these two subclusters are extended along the direction of the Perseus-Pegasus supercluster, and we suggest that Abell 2626 is preferentially accreting subclusters and groups from this large-scale structure filament. We also find an extended X-ray source associated with the cluster S0 galaxy IC 5337; the morphology of this source suggests that it is infalling from the west, and is not associated with the southwest subcluster, as had been previously suggested.

*Subject headings:* cooling flows — galaxies: clusters: general — galaxies: clusters: individual (Abell 2626) — intergalactic medium — radio continuum: galaxies — X-rays: galaxies: clusters

1. INTRODUCTION

The central regions of clusters of galaxies are among the most interesting and physically active areas in the Universe. In many clusters of galaxies, there is a central peak in X-ray surface brightness, with a central cooling time which is less than the age of the cluster (e.g., Chen et al. 2007). In the classical cooling flow picture, the rapid cooling of gas in this region leads to the loss of central pressure (Fabian 1994). If there is no additional heating, the cooled gas would flow into the center in a cooling flow. The gas should continue to cool to very low temperatures. However, recent high resolution X-ray spectra from *XMM-Newton* and *Chandra* show that there is not enough cooler X-ray gas to be consistent with a classical cooling flow (Peterson et al. 2001, 2003; Peterson & Fabian 2006).

The lack of sufficient cooler materials probably means that there is an additional heating source within the central cooling core region. Very often, the clusters host central dominant galaxies which are also strong radio sources. In some of the clusters, there is strong evidence that the central radio sources are interacting with the surrounding X-ray emitting plasma. The radio sources blow “bubbles” in the X-ray emitting gas, displacing the gas and compressing it into shells around the radio lobes.

At the same time, the radio sources are confined by the X-ray emitting gas (Fabian et al. 2000; Blanton et al. 2001). In some clusters, “ghost bubbles” at larger radii are seen which are weak in radio emission except at low frequencies (McNamara et al. 2001; Clarke et al. 2005). They are believed to be previous eruptions of the radio sources, which are episodic. In some cases, buoyantly rising bubbles may entrain cooler X-ray gas from the centers of the cooling cores (Churazov et al. 2001; Fujita et al. 2002, 2004). Some radio sources previously classified as cluster merger radio relics may actually be displaced radio bubbles from the central radio sources (Fujita et al. 2002, 2004). In some recent studies, there is even evidence of radio jets restarted at a different position angle from a previous outburst, which may be due to a precessing supermassive blackhole (Gitti et al. 2006). With high resolution 3D simulations, Vernaleo & Reynolds (2006) have shown that multiple bursts from the AGN along the same direction fail to produce a long-term balance of heating and cooling. The reason is that a low-density channel is evacuated by a previous jet, while the subsequent jets can pass through the channel freely without heating the cooling core region. It has been suggested that jet precession is a possible solution to this problem. Alternatively, turbulence, rotation, or bulk motions in the intracluster medium (ICM) might also move or disrupt the channel made by the radio source, and keep the energy from just going down the same channel (e.g., Heinz et al. 2006).

Abell 2626 ( $z = 0.0573$ , Abell et al. 1989) hosts a moderate cooling flow of  $\sim 50 M_{\odot} \text{ yr}^{-1}$  based on *Einstein* data (White et al. 1997). A double nuclei cD galaxy is

<sup>1</sup> Department of Astronomy, University of Virginia, P. O. Box 400325, Charlottesville, VA 22904-4325, USA; kw Wong@virginia.edu, sarazin@virginia.edu

<sup>2</sup> Institute for Astrophysical Research, Boston University, 725 Commonwealth Ave., Boston, MA 02215, USA; eblanton@bu.edu

<sup>3</sup> Argelander-Institut für Astronomie, Universität Bonn, Auf dem Hügel 71, D-53121 Bonn, Germany; thomas@reiprich.net

sitting at the center of the cluster. From high resolution VLA images, Gitti et al. (2004) recognized that there is an unresolved radio core coincident with the central cD galaxy. There is a small jet-like feature extended towards the southwest direction from the unresolved radio core. In addition, there are two unusual amorphous, symmetric radio “bars” running parallel at opposite sides of the central cD galaxy. These compact features are distinct from and embedded in diffuse extended radio emission (a mini-halo). Gitti et al. (2004) believed that the radio bars may represent an earlier evolutionary stage of jets injected by the central source. Thus, Abell 2626 is a good candidate for studying the interaction between the X-ray emitting intracluster medium and the radio emitting plasma (Rizza et al. 2000; Gitti et al. 2004; Marković et al. 2004). Previous *ROSAT* X-ray and VLA radio observations suggested that there is an X-ray excess which is spatially correlated with the radio source, but failed to find strong X-ray deficits (holes) in Abell 2626 (Rizza et al. 2000). Rizza et al. (2000) carried out numerical simulations, and showed that even a weak jet (internal Mach number = 5) should produce a significant hole along the line-of-sight to the radio jet. They suggested that the lack of X-ray holes may be due to mixing of thermal and radio plasma in the region, although their numerical simulations did not distinguish between these two components. They also ran simulations in which the jet turned off, which resembled the observations of weak X-ray holes. Another possibility they noted is the imprecise model they used to subtract out from the symmetric X-ray emission to obtain a residual image. They searched for X-ray and radio correlations from the residual image but failed to find strong X-ray deficits (holes) displaced by the radio plasma. With the excellent spatial resolution provided by *Chandra* and deeper observations provided by both *Chandra* and *XMM-Newton*, we are able to study the complicated central region of Abell 2626 in more detail.

While many radio sources are associated with AGNs in cluster galaxies, there exist other types of extended radio emission associated with the diffuse intracluster medium without clear galaxy hosts. These extended radio sources can be divided into cluster-wide halos, relics, and mini-halos (Feretti & Giovannini 1996, 2007). Abell 2626 contains a candidate mini-halo (Gitti et al. 2004). Cluster-wide halos and relics are large in scale ( $\sim 1$  Mpc), with halos located in the centers of clusters, while the relics are generally located at the periphery. Very often, these two types of large scale diffuse radio emission are found in clusters without cooling cores. This indicates a possible origin in cluster mergers, which are believed to disrupt cooling cores and to re-accelerate radio-emitting particles (Brunetti 2004; Blasi et al. 2007). However, some cooling core clusters with dominant radio galaxies host mini-halos at the cluster center with extended radio emission up to 0.5 Mpc. The morphology of the mini-halos is different from that of the radio bubbles at the centers of many cool core clusters, which show a strong X-ray/radio interaction in which the radio lobes displace X-ray gas. This hints at a different transport mechanism (not jets) to explain the extended property of the mini-halos. The typical time scales for radiative losses by relativistic electrons ( $\sim 10^7 - 10^8$  yr) in cooling cores with strong magnetic fields are much shorter than the

diffusion times ( $\sim 10^9$  yr) for the electrons to be transported from the center of the cooling core out to a fraction of a Mpc. Hence, the diffuse radio emission from mini-halos suggests that an *in-situ* re-acceleration mechanism is needed for the electrons. The origin of the mini-halos has remained unclear, but it has been suggested that the interaction of the central radio galaxy and the intracluster medium (re-)accelerates particles to relativistic energies. Recently, Gitti et al. (2004) modeled Abell 2626 with an electron re-acceleration model driven by MHD turbulence amplified by the compression of the magnetic field in the cooling core region. They have shown that the model agrees with various observational constraints such as the observed radio brightness profile, the integrated synchrotron spectrum, and the radial steepening of the radio spectrum. They conclude that only a tiny fraction ( $\sim 0.7\%$ ) of the maximum power that could be extracted from the cooling core (based on the standard cooling flow model) is needed for re-acceleration. Since the re-acceleration model for the origin of the mini-halo assumes a physical connection between thermal and relativistic plasma, it is essential to perform new X-ray observation to derive accurately the properties of the ICM (e.g., cooling radius, mass accretion rate, as well as morphology of the X-ray emission). On another hand, Pfrommer & Enßlin (2004) suggested that the re-acceleration is of hadronic origin which should be best tested by  $\gamma$ -ray observations.

In this paper, we present a detailed study of Abell 2626 from *XMM-Newton* and *Chandra* observations focused on the X-ray and radio interaction. The paper is organized as follows. In § 2, we describe observations and data reduction. The X-ray images are analyzed in § 3, with an emphasis on the X-ray morphology of the overall region, the central region, and the S0 galaxy IC 5337 in § 3.1. In particular, two extended X-ray emission regions possibly associated with subclusters are discussed in § 3.1.1. The point sources detected in the X-ray data are discussed in § 3.2. The X-ray surface brightness profile is studied in § 3.3. Various substructures identified on residual maps are presented in § 3.4. Spectral analysis is presented in § 4. In particular, cluster profiles, mass deposition rate, cooling and thermal conduction time scales, hardness ratio maps, possible AGNs associated with the cD galaxy IC 5338 and the S0 galaxy IC 5337 are discussed in this section. Throughout the data analysis sections (§§ 3 & 4), some discussions related to the interpretation of the results are presented to help readers understand the data. We then discuss the kinematics of the S0 galaxy and the cooling flow interaction with the central radio source in §§ 5 & 6 in detail, respectively. We summarize our work in § 7. We assume  $H_0 = 71$  km s $^{-1}$  Mpc $^{-1}$ ,  $\Omega_M = 0.27$  and  $\Omega_\Lambda = 0.73$  throughout the paper. At a redshift  $z = 0.0573$ , the luminosity distance of Abell 2626 is 252.8 Mpc, and  $1'' = 1.10$  kpc. The virial radius is approximately 1.53 Mpc (Markevitch et al. 1998) for the average cluster temperature of  $T_X = 3.0$  keV (White et al. 1997).

## 2. OBSERVATIONS AND DATA REDUCTION

### 2.1. *XMM-Newton* Data

Abell 2626 was observed (Obs. ID 0148310101) on 2002 December 28 by *XMM-Newton* for  $\sim 38$  and  $\sim 42$  ks with

the EPIC PN and MOS cameras, respectively. Extended Full Frame mode (PN) and Full Frame mode (MOS) were used with thin optical filters. *XMM-Newton* data reduction was done with SAS version 5.4.1. All the data were reprocessed using the tasks *epchain* and *emchain*. We included only events with FLAG=0 in our analysis. We chose only events with PATTERN = 0-4 (0-12) for PN (MOS) data.

Background flares were rejected by performing a  $2\sigma$  clipping of the 100 s binned light curves in the 12-14 keV and 10-12 keV band for the PN and MOS cameras, respectively, which yielded the out-of-time corrected exposure times of 35,563 s, 40,300 s and 40,600 s of cleaned data for the PN, MOS1 and MOS2 cameras, respectively. Blank-sky background files collected by D. Lumb<sup>4</sup> were used during the analysis. The observed background levels, estimated from the total count rate in the whole field of view in the hard band (10 – 12 keV and 12 – 14 keV for MOS and PN, respectively), are 1.07, 0.99 and 1.26 times those in the blank-sky backgrounds for MOS1, MOS2 and PN, respectively. We have renormalized the blank-sky backgrounds accordingly. The uncertainty of the PN background is larger than that for the MOS detectors. The effect of the larger PN background uncertainty and some other background uncertainties on the spectral analysis are addressed in § 4.1.1. The image and hardness ratio map analyses were done using the MOS data only (§§ 3 & 4.6), and we checked that the results of the analysis would not be affected by a change in the background normalization of  $\pm 10\%$ . The vignetting effect for the image and hardness ratio map analysis has been corrected using the exposure maps.

## 2.2. *Chandra* Data

A *Chandra* observation (Obs. ID 3192) of  $\sim 25$  ks was made on 2003 January 22 in Very Faint mode. The center of the cluster was positioned  $3'$  from the edge of the S3 chip (midway between the node boundaries). The focal plane temperature was  $-120$  C.

The *Chandra* data reduction was done with CIAO version 3.1, using calibration products from CALDB 2.28. The latest gain file (CALDB GAIN 2.28) and geometry file (CALDB 2.9) at the time of reduction were used. The reduction was done in Very Faint mode to remove more particle background. Background flares were rejected by performing the standard clipping using the *lc\_clean* routine written by M. Markevitch<sup>5</sup>. This yielded 22,959 s of cleaned data. Since the whole field-of-view is dominated by the cluster X-ray emission, internal background cannot be used. The blank-sky background files collected by M. Markevitch were used during the analysis. The difference between the observed and the blank-sky high energy (9–12 keV) background count rates was less than 1%, and this small difference was removed by renormalizing the background. The influence of the background on the spectral fitted measurements (temperature profile) has been checked by varying the background normalizations by  $\pm 10\%$ , and the results are not significantly changed. To check if there might be a significant difference between the Galactic background in the source and blank-sky observations, another thermal component

with a fixed low temperature of 0.2 keV has been added (Markevitch et al. 2003; Lumb et al. 2002). Normalization of the additional component has been allowed to be negative for the case of more Galactic emission in the blank-sky observations compared to the cluster observation. All the results are basically unchanged. Fixing the temperature of the additional component to be the outermost temperature that can be determined from the *Chandra* field of view also gives essentially the same results. We conclude that the *Chandra* results are insensitive to uncertainties in the background.

## 3. X-RAY IMAGE ANALYSIS

### 3.1. *X-ray Morphology*

#### 3.1.1. *Global morphology*

The background subtracted, exposure-corrected, adaptively smoothed mosaic of the *XMM-Newton* EPIC MOS1 and MOS2 images is shown in Figure 1. The PN image was not included because of its different spectral response and because the chip gaps and bad columns produced cosmetic artifacts in the smoothed image. The image was smoothed to a signal-to-noise ratio of 3 per smoothing beam.

The global X-ray image of Abell 2626 appears to be roughly azimuthally symmetric. The brightest region at the center corresponds to the position of the cD galaxy IC 5338. There is a source associated with the cluster S0 galaxy IC 5337 which is  $1/3$  west of the center of the cluster. Excess X-ray emission is seen to the southwest of the cluster, extending from  $\sim 1'$  out to  $\sim 7'$  (see § 3.4). Mohr et al. (1996) identified a subcluster to the southwest of this region based on optical observations of the galaxy population. The subcluster identified is centered roughly at the southwest edge of the *XMM-Newton* field of view, but the distribution of the galaxies covers a region where the excess X-ray emission is seen. Mohr et al. (1996) show that the subcluster is bound to and falling into the main cluster. Our *XMM-Newton* image shows, for the first time, extended X-ray emission possibly associated with the subcluster in the southwest direction. The extended X-ray emission can be viewed on a background subtracted, exposure corrected, adaptively smoothed image. The location of the extended emission possibly associated with the subcluster is circled at the southwest corner in Figure 1. The extended emission at the southwest corner is not obvious, but the slight deviation from spherical symmetry in that region can be noted. The shape of the extended emission region is difficult to characterize due to the low signal-to-noise ratio near the edge of the cluster. By inspecting various images, we chose a circular region centered on the highest excess X-ray emission, with a radius chosen to be small enough so that the region did not overlap with the nearly circular cluster emission of Abell 2626. Our choice for this region is justified by the hardness ratio map below (Figure 14) which shows that the extended region chosen appears to be harder than its surrounding. Compared to the X-ray emission at the same radius from the main cluster center (the cD galaxy IC 5338) with all point sources and other extended emission excluded, the excess emission is significant at the  $4.6\sigma$  level. Our residual images (§ 3.4 below) also indicate the possible signatures of a merger.

Another extended X-ray source can be seen about  $7'$

<sup>4</sup> <http://xmm.vilspa.esa.es/pub/ccf/constituents/extras/background/>

<sup>5</sup> <http://cxc.harvard.edu/contrib/maxim/acisbg/>

northeast of the center of Abell 2626 (Figure 1). The criteria used to define the northeast region are the same as the southwest one. This feature is significant at the  $11.6\sigma$  level. It should be noted that there is a chip gap at about  $5'.5$  from the center which makes the extended X-ray source appear to be more distinct than it actually is. No cluster or group structure has been identified previously in this region. However, Abell 2626 is known to be associated with the Perseus-Pegasus supercluster, a filament of clusters of galaxies extending for as much as  $\sim 300$  Mpc (Batuski & Burns 1985a,b; Zucca et al. 1993; Einasto et al. 2001). The southwest to northeast extension to the structure in our X-ray image around Abell 2626 is elongated along the Perseus-Pegasus filament. This may indicate that the cluster is preferentially accreting subclusters and groups from this supercluster.

### 3.1.2. Central Region

The background subtracted, exposure corrected, adaptively smoothed *Chandra* image of the central  $3'.5 \times 2'.4$  is shown in Figure 2 (left panel). The image was smoothed to a signal-to-noise ratio of 3. The brightest region of the X-ray emission in the cluster is centered on the southwest nucleus of the central cD galaxy. This source is possibly extended in both soft (0.3–2 keV) and full band (0.3–10 keV) images when detected by *wavedetect* in CIAO, but nothing was found by *wavedetect* in the hard band (2–10 keV). However, examination of the raw soft band (0.3–2 keV) image shows two peaks superposed on the two optical nuclei of the central cD galaxy (lower left panel of Figure 3). There is also a hard point source seen in the raw hard band (2–10 keV) image (lower right panel of Figure 3). The position of this hard point source agrees with the southwest cD nucleus. The hard point source is separated from the peak of the radio core by less than  $1''$ . This source can also be seen in the hardness ratio map (Figure 16 below). The hard point source and its likely association with the AGN at the center of the southwest cD nucleus and radio core are discussed further in § 4.7. This source is located along an arc of X-ray emission extending from the northeast to the west to the south of the cluster center.

Previous *ROSAT* X-ray and VLA radio observations suggest that there is enhanced X-ray emission spatially coincident with the radio source (Rizza et al. 2000). In Figure 2 (left panel), the contours from the VLA 1.5 GHz B-array radio image are shown in green (Gitti et al. 2004). The position of the radio core agrees with the brightest region of X-ray emission. In particular, the radio core is centered at the southwest cD nucleus rather than the northeast one. There is an arc of X-ray emission which may correspond to the curved radio jet feature to the south of the core.

However, the most unusual features of the radio image are the two elongated radio bars to the north and south of the radio core. We find there is no obvious correlation between the two radio bars and the *Chandra* X-ray image in Figure 2 (left panel). No obvious X-ray deficit (holes) is found on the *Chandra* X-ray image, which is consistent with the finding of Rizza et al. (2000). We have generated residual maps to further investigate our finding, and the results will be presented in § 3.4. Our interpretation is that the radio bars are thin tubes (see

§ 6 below).

One interesting feature is that there is an X-ray excess “tongue” which extends from the central cD galaxy to the southern radio bar, and there is a similar but weaker tongue in the northern direction as well (upper right panel of Figure 3). The tongues are best seen in the residual map in Figure 8 of § 3.4.

Figure 2 (left panel) also shows radio contours (white) from the VLA 1.5 GHz C-array (Gitti et al. 2004) overlaid on the *Chandra* image showing the radio mini-halo in Abell 2626. The mini-halo is roughly confined within  $60''$  with a diamond shape. The distance from the center to the NE or SW corners of the diamond is about  $50''$ , while to the NW or SE corners it is about  $70''$ . A discussion on the mini-halo will be presented in § 6.

### 3.1.3. The S0 Radio Galaxy IC 5337

About  $1'.3$  west of the central cD galaxy, there is an X-ray source associated with the S0 galaxy IC 5337 (left panel of Figure 2). This source is clearly extended in the soft band image, but a hard band image shows that there is a point source coincident with the nucleus of IC 5337. The possibility that the S0 nucleus is an AGN will be discussed below (§ 4.7). To the south of IC 5337, there is another X-ray point source which is not associated with any known galaxy. As indicated in Figure 2, there is a nearby radio source which may be associated with this X-ray source.

The right panel of Figure 2 shows the bow-shock-like shape of the extended X-ray emission associated with the S0 galaxy IC 5337. The image is created by removing and replacing the southern point source by the average surrounding X-ray intensity, and then adaptively smoothing to a signal-to-noise ratio of 4.

The S0 galaxy IC 5337 also is a radio source (Figure 2). Radio contours (Gitti et al. 2004) are overlaid in Figure 2 (right panel). There is a component centered on the S0 galaxy, and a component located at a position of about  $190^\circ$  (measured from north to east) of the S0 galaxy on the 1.5 GHz B-array map. The 1.5 GHz C-array map shows three radio tails in the south, southwest and west directions. The kinematics of the S0 galaxy will be discussed in § 5.

### 3.2. Source Detection

We used the *XMM SAS* task *eboxdetect* to detect a total of 90 distinct point sources on the *XMM* images; the detections were done separately on each of the three detectors, and then the source lists were combined. The sources were confirmed by inspection, and some low-level detections at the edge of the FOV or bad pixel gaps were removed. Here we discuss only the sources with possible optical counterparts within  $20''$ . In fact all optical counterparts identified are within  $11''$ . We adopt the NED source with an accurate position which is closest to the X-ray position. The possible associations of X-ray point sources with AGNs in the central cD galaxy IC 5338 and the S0 galaxy IC 5337 were noted above (§§ 3.1.2 & 3.1.3), and will be discussed in more detail below (§ 4.7). Nine X-ray sources are included in the list (Table 1). Figure 4 is an optical image from the Digital Sky Survey with the 9 X-ray sources marked. Two of these are the central cD galaxy IC 5338 and the S0 galaxy IC 5337

discussed above. Interestingly, three of the X-ray sources correspond to galaxies which are located in the region of extended X-ray emission about  $7'$  northeast of the center of Abell 2626 (Figure 1). However, one of these possible optical IDs (2MASX J23365722+2114032) has a redshift of 0.038, and thus is not directly associated with Abell 2626.

On the *Chandra* image, 14 point sources were detected by *wavedetect* in CIAO using the default settings. Of these, only the central cD IC 5338 galaxy and the S0 galaxy IC 5337 have possible identifications in NED with positions that agree with the X-ray to within  $10''$ . Table 2 lists the positions of the 14 *Chandra* X-ray point sources. Figure 5 is an optical image from the Digital Sky Survey with the locations of the 14 X-ray sources marked.

Unless specified, all the sources detected are excluded in the analysis of extended emissions in the subsequent sections.

### 3.3. Surface Brightness Profile

The azimuthally-averaged X-ray surface brightness profile was extracted separately for the *Chandra* and *XMM-Newton* data. Except for the two extended X-ray clumps to the NE and SW and the structure in the very center, Abell 2626 appears to be a nearly relaxed cluster. The profiles were fitted using a double beta model profile of the form

$$S(r) = \sum_{i=1,2} S_i(0) \left[ 1 + \left( \frac{r}{r_{ci}} \right)^2 \right]^{-3\beta_i+1/2}, \quad (1)$$

which has been shown to provide a good fit to relaxed clusters with cooling cores (Xue & Wu 2000).

The background subtracted and exposure corrected surface brightness profile from the *XMM-Newton* MOS1 and MOS2 data is shown in Figure 6. The PN data were not included since the spectral response is different which complicates the deprojection of the electron density profile below (§ 4.3). Also, the fitted surface brightness model was used to create residual images (§ 3.4 below), and including the PN image would produce cosmetic artifacts due to the larger chip gaps and greater number of bad columns in the PN camera. All of the X-ray point sources except the central cD galaxy were excluded from the data. The extended X-ray emission around the S0 galaxy was also excluded, as it produced a feature in the cluster surface brightness profile. We also excluded the extended X-ray emission regions to the NE and SW of the cluster which were described in and the criteria of defining the regions were explained in § 3.1.1. The annuli were chosen such that all the widths are larger than the FWHM of the PSF at that radius. With this choice, all the bins contain at least 1000 counts after background subtraction for the *XMM-Newton* MOS1 and MOS2 data. With these very good statistics, the error bars on the surface brightness are too small to be easily seen in the top panel of Figure 6; instead, we present the residuals in the lower panel. The parameters of the best-fit double beta model are  $S_1(0) = 0.40^{+0.02}_{-0.02}$  and  $S_2(0) = 0.10^{+0.01}_{-0.01}$  counts  $s^{-1}$  arcmin $^{-2}$ ,  $r_1 = 34.8^{+7.1}_{-5.6}$  and  $r_2 = 128.5^{+8.1}_{-7.2}$  arcsec, and  $\beta_1 = 0.91^{+0.26}_{-0.18}$  and  $\beta_2 = 0.73^{+0.02}_{-0.01}$ . Visually, the double beta model fit seems

adequate. However, with the very small errors on the measured surface brightness, the fit is actually not very good, with a reduced  $\chi^2$  of 2.3. In addition to the excess at the center, associated with the central cD galaxy and radio source, within  $200''$  there are several other regions of excess or deficient emission compared to the model. These features are reproduced (albeit with poorer statistics) in the *Chandra* surface brightness data, and in the data from the *XMM-Newton* PN detector. These residuals may indicate that the central region is disturbed by effects of the central radio source beyond the current extent of the source, or that the cluster is not completely relaxed due to a merger.

### 3.4. Residual Images

To better understand the origin of the residuals in the surface brightness fit and the dynamics of the intracluster gas, we created residual maps for both *XMM-Newton* and *Chandra* images (Figures 7 and 8). Simulated azimuthally-symmetric X-ray images were produced which exactly followed the double beta model fits to the surface brightness. These simulated images were subtracted from the adaptively smoothed images. Figure 7 shows the *XMM-Newton* and *Chandra* residual images with the same field of view. Both residual maps show similar structures; the *XMM-Newton* image has great contrast due to the better statistics, while the *Chandra* image shows more detailed structures. Substructures can be identified with many of the residuals seen in the maps. A large region of excess emission can be seen about  $110''$  southwest of the cD galaxy, which corresponds to the peak of the surface brightness residuals around that radius. Other regions of excess and deficit within  $100''$  can also be identified from the residual map of the *Chandra* image (right panel of Figure 7). In the surface brightness residuals, the central excess corresponds to the central bright point in Figure 7 (right panel). The trough around  $15''$  corresponds to the dark ring around the central excess in the residual map which can be seen more clearly on Figure 8. The peak at around  $30''$  is probably due to the two bright regions due north and south in the residual map (labeled as two green circles). The trough around  $50''$  corresponds to the dark region indicated by a white polygon in the residual map. The peak around  $110''$  corresponds to the far southwest excess labeled with a green polygon in the residual map.

Most of the structures in the inner region occur on a scale similar to that of the radio sources in the center. In order to study the radio/X-ray interaction in more detail, Figure 8 shows radio contours from the VLA 1.5 GHz C-array (white contours) and the 1.5 GHz B-array radio images (green contours, Gitti et al. 2004), overlaid on the central part of the *Chandra* residual map. In general, the diamond-shaped outline of the extended radio emission (the radio “mini-halo”) corresponds to a region of reduced X-ray emission, and there are excess X-ray regions NNE and SSW of the edge of the mini-halo where the radio surface brightness is dropping rapidly. The mini-halo is roughly confined within  $60''$ . The distance from the center to the NE or SW corners of the diamond is about  $50''$ ; while to the NW or SE corners is about  $70''$ . Note that in the interpretation of Gitti et al. (2004), the two radio bars are distinct from the diffuse radio emission, and in fact after their subtraction the

morphology of the mini-halo becomes roughly circular (see Figure 6 of Gitti et al. 2004). However, in the residual image in Gitti et al. (2004), we can still see some excess radio emission in the NW and SE corners. As noted previously, there is a significant excess associated with the radio core and the southern radio jet. The southern radio bar is a region of X-ray excess, but the northern bar shows an excess to the east and a deficit to the west in X-rays. The interpretation of the interaction between thermal and radio plasma will be discussed in § 6 in detail.

The one major X-ray residual in the inner cluster which is not on the scale of the central radio emission is the extended excess to the SW. It is possible that this has been produced by the action of the central radio source. However, the SW excess is between the cD galaxy and the subcluster southwest of the main cluster center. It is possible that this excess is the result of this merger or a previous merger from this direction. There is no obvious sharp surface brightness discontinuity associated with this excess, which means that it either is not a shock or cold front, or that the merger is not occurring primarily in the plane of the sky. We note that Mohr et al. (1996) show that the line-of-sight velocity difference between the main cluster and the subcluster is  $\sim 2600 \text{ km s}^{-1}$ , which is greater than the typical sound speed within clusters. If the excess is the result of a merger, this suggests that the merger is mainly along the line-of-sight.

#### 4. SPECTRAL ANALYSIS

##### 4.1. Temperature Profile

The azimuthally averaged, projected temperature profile for Abell 2626 was extracted using both *XMM-Newton* and *Chandra* data (upper panel of Figure 9). The spectra were fitted using an absorbed thermal model (WABS\*MEKAL) with XSPEC Version 12.3.1. For the *XMM-Newton* data, all the spectra of the three cameras were fitted simultaneously. The energy bands used are 0.6-10.0 and 0.4-7.0 keV for *XMM-Newton* and *Chandra* data, respectively. Using 0.6-7.0 keV and 0.5-10.0 keV bands for *XMM-Newton* and *Chandra* data gives essentially the same results. The spectra were grouped to have a minimum of 25 counts per bin. We fixed the absorption to be  $4.2 \times 10^{20} \text{ cm}^{-2}$  (Dickey & Lockman 1990) and the redshift to be 0.0573 (Abell et al. 1989). Freeing these values gives essentially the same results. Except the outermost data point where the reduced  $\chi^2$  value is  $\sim 1.6$ , all the other reduced  $\chi^2$  values are  $\lesssim 1$ , which indicates that the fits are good. To ensure that the spectra are not affected by energy-dependent PSF effects, the annuli of the *XMM-Newton* data were chosen such that all of the widths are at least twice the PSF half energy width of the PN camera.

The general trend is that the projected temperature increases from a central value of  $\sim 2.5 \text{ keV}$  within  $9''$  ( $\sim 10 \text{ kpc}$ ) to a maximum of  $\sim 3.5 \text{ keV}$  at  $100'' - 200''$  ( $110 - 220 \text{ kpc}$ ). Such a radial increase is normally seen in a cluster cooling core. The projected temperature then decreases to  $\sim 1.4 \text{ keV}$  at  $\sim 540''$  ( $\sim 600 \text{ kpc}$ ). Interestingly, there is a sharp drop in the projected temperature from  $\sim 2.9 \text{ keV}$  at  $210''$  ( $230 \text{ kpc}$ ) to  $\sim 2.0 \text{ keV}$  at  $270''$  ( $296 \text{ kpc}$ ) in the *XMM-Newton* data. Outside of this steep drop, the projected temperature gradient flat-

tens. The radius of the drop corresponds to the distance from the cD galaxy to the outer edge of the large excess emission in the southwest direction. If the large excess emission indicates a merger signature, the temperature jump might indicate that gas is heated within that region. Unfortunately, the jump cannot be confirmed with *Chandra* as the *Chandra* data does not extend far enough in all directions to reach the distance of the jump seen in the azimuthally averaged temperature profile. It only extends far enough towards the northwest direction, where there are not enough counts to constrain the temperature.

In general, the *XMM-Newton* data give lower values for the projected temperature profile. There are at least three possible explanations for this difference. First, it might be due to the larger PSF of *XMM-Newton*. The softer photons from the brighter, cooler inner regions may be scattered to outer regions, hence making the outer regions appear cooler. This effect may be seen from the second bin outward, and should be more serious in regions where the gradient of the surface brightness is greatest (i.e., near the center; Markevitch 2002). This might explain the discrepancy in the second and third bins of our *XMM-Newton* data. The second possibility is that there might have been a steady and mild enhancement in the hard X-ray background during the *Chandra* observation which was not removed by the standard cleaning procedure; this could make the *Chandra* emission appear hotter, particularly in outer, low surface brightness regions. Such an effect has also been noted by Markevitch (2002). We have tried to assess the importance of such a background enhancement by including a component for the hard background, modeled as a power law with an exponential cutoff (Markevitch 2002; Markevitch et al. 2003) in the fits of the *Chandra* spectra. However, this component did not significantly improve the fits, and the best-fit amplitude of the component was negligible. A third possibility is that the continuous accumulation of the contaminant layer on the *Chandra* ACIS optical blocking filter was underestimated.

To study the true temperature of the cluster, we have also deprojected the temperature profile by using the XSPEC PROJCT model. For each annulus, the model sums up the appropriate fractions of emissions contributed from the outer annuli. The spectra of all the annuli were fitted simultaneously to get the deprojected temperature profile. The middle panel of Figure 9 shows the azimuthally averaged, deprojected temperature profile for Abell 2626 using both *XMM-Newton* and *Chandra* data. For the *XMM-Newton* data, all the spectra from the three cameras were fitted simultaneously. The *XMM-Newton* and *Chandra* data are consistent within the 90% confidence uncertainties, but the uncertainties of the *Chandra* data are much larger. Since the *XMM-Newton* data extends further out and has smaller error bars, we describe results obtained from the *XMM-Newton* in the following. We also adopt the *XMM-Newton* spectral fits (lower panel of Figure 9) for the deprojection and the mass profile analysis below (§§ 4.3, 4.4, & 4.5).

The deprojected central temperature is slightly lower than the projected one because the latter is contaminated by the hotter emission along the line of sight. The difference is small since the hottest region has a temperature only 1 keV higher than the central one. A more notice-

able difference is that the temperature jump at around  $240''$  is more obvious in the deprojected profile. It drops from a temperature of  $\sim 3.5$  keV to  $\sim 2.2$  keV. The peak of the deprojected temperature profile is located just within the temperature jump ( $\sim 180 - 240''$ ).

#### 4.1.1. Effects of XMM Background Uncertainties

Since the cluster emission covers the whole field of view and the correct background cannot be estimated easily, the so called “double background subtraction” method, common in *XMM-Newton* data analysis (Arnaud et al. 2002), cannot be applied. The natural background subtraction method is to perform a renormalized blank-sky background subtraction without the second step of extracting a blank-field-subtracted spectrum in an emission free region in the “double background subtraction” method. We use this “single background subtraction” method. Note that this method has also been applied to the study of a cluster with a similar redshift to Abell 2626 (Arnaud et al. 2001). As mentioned in Arnaud et al. (2001), our treatment does properly account for the cosmic-ray (CR) induced background. However, the contributions from variations in the local soft Galactic background (which depends on the position on the sky) and the extragalactic X-ray background component (which depends on the absorbing hydrogen column density along the line of sight and cosmic variance) were not included. In our case, the emission from Abell 2626 usually dominates the local soft Galactic background, and the CR induced background usually dominates the hard X-ray extragalactic background component. Using the ROSAT All Sky Survey (Snowden et al. 1997), we have compared the soft X-ray emission (0.47–1.21 keV) around Abell 2626, and the exposure-weighted emission in the regions used to extract the blank-sky background, and the difference is less than 4%. The hydrogen column density towards Abell 2626 is about a factor of two higher than that for most of the blank-sky fields (Dickey & Lockman 1990), but is not high enough to affect the cosmic X-ray background strongly. Also, as mentioned previously, the CR induced background usually dominates the hard X-ray extragalactic background component. Hence, the blank-sky backgrounds should represent the soft Galactic background and the hard X-ray background reasonably.

We were concerned that, while the background renormalizations for MOS1 and MOS2 are modest ( $\lesssim 7\%$  correction), the renormalization of the PN background is larger ( $\sim 26\%$  correction). While the uncertainties in the background will affect most strongly the derived temperatures of the outer regions of the cluster, we emphasize here that most of our focus in this paper is on the X-ray and radio interaction in the innermost region where the results are nearly independent of background assumed. We performed a number of tests to address the effects of the *XMM-Newton* background uncertainties on the deprojected temperature profiles. We did this by: 1) varying the blank-sky background normalizations by  $\pm 10\%$  ( $\pm 20\%$ ) for the MOS (PN); 2) using the blank-sky backgrounds without renormalization; 3) using the MOS1+MOS2 spectra only; 4) using the PN spectra only; 5) adding an extra 0.2 keV MEKAL component (with normalization free and allowed to be negative in each annulus) as a model for any variation in the soft Galactic component. The test results are summarized in

Figure 10. Our adopted deprojected temperature profile in this paper is shown in black diamonds.

Within  $r < 180''$ , all the deprojected temperatures are in very good agreement. All these tests show a significant jump in temperature near  $240''$  and a flattening of temperature beyond this jump. As expected, increasing the background normalization (blue diamonds) gave lower deprojected temperatures for the outer regions ( $r > 180''$ ), while decreasing the background normalization (green diamonds) gave higher temperature. Using the blank-sky backgrounds without renormalization (red crosses) also gave higher temperatures (green diamonds). The variation in the temperatures using different normalizations was at most  $\sim 1$  keV in the outer region.

The deprojected temperature profiles obtained from the MOS1+MOS2+PN spectra (black diamonds), the MOS1+MOS2 spectra (magenta triangles), and the PN spectra alone (cyan triangles) all agree reasonably well. Thus, the PN data appear to give fairly reliable spectral information, even though the uncertainty in the PN background normalization may be larger.

Finally, varying the amount of soft Galactic background (orange crosses) gave deprojected temperatures in good agreement with those using the renormalized blank sky backgrounds (black diamonds) except for the outermost annulus. The large deviation of the outermost data point may indicate that there is less of soft Galactic emission in the direction of Abell 2626 than in the blank-sky fields because the fitted normalization of the extra soft Galactic background component in the model is negative. The soft Galactic component should be uniform on the scale of a cluster. However, a reduction in the soft Galactic background similar to that suggested by the last annulus was found to be completely inconsistent with the fits in the inner annuli. Hence, we concluded that the reduced soft component in the outermost annulus was not due to a reduction in the soft Galactic background towards the cluster. The reduced soft component in the outermost annulus may be the result of additional thermal structure in this region.

To summarize, all our results are independent of background used within  $\sim 180''$ . For the outer regions, the temperature profile is only slightly affected by the choice of the background, but the differences are mostly well within the error bars. All the features described in the paper related to temperature measurements (e.g., the temperature jump, pressure, entropy profiles, etc.) are not affected.

#### 4.2. Central X-ray Spectrum and Cooling Rate

We determined the radiative cooling rate by fitting the X-ray spectrum of the central regions of the cluster from both *XMM-Newton* and *Chandra* data. We extracted the spectrum from a circular region with a radius of  $65''$ , which is roughly the cooling radius determined in § 4.4 below. In XSPEC, we used the WABS\*(MKCFLOW+MEKAL) model, which combines a cooling flow component (MKCFLOW) with an isothermal model (MEKAL) to account for the gas in the outer regions. The absorption was fixed at the Galactic column of  $4.2 \times 10^{20}$  cm $^{-2}$  as before. The upper temperature ( $kT_{\text{high}}$ ) and abundance of the MKCFLOW component was set to be the same as the MEKAL component,

which is expected if the gas cooled from the ambient ICM. Initially, the lower temperature of the MKCFLOW component is set to be the lower limit for the model ( $kT_{\text{low}} = 0.08$  keV), as expected for the classical cooling flow model in which the gas cools radiatively to very low temperatures. With this assumption, the best-fit cooling mass deposition rate is  $2 \pm 1$  ( $3 \pm 3$ )  $M_{\odot} \text{ yr}^{-1}$  for *XMM-Newton* (*Chandra*) data in the 0.6–10.0 (0.5–7.0) keV energy band with a  $\chi^2/dof = 1.18$  (0.90). The fitted upper temperature and abundance were  $kT_{\text{high}} = 2.8 \pm 0.05$  ( $3.3 \pm 0.2$ ) keV and  $0.52 \pm 0.03$  ( $0.9 \pm 0.1$ ) solar, respectively. Allowing  $kT_{\text{low}}$  to vary increased the mass deposition rate to be  $74 \pm 6 M_{\odot} \text{ yr}^{-1}$  for the *XMM-Newton* data, with  $kT_{\text{low}} = 1.5 \pm 0.1$  keV,  $kT_{\text{high}} = 4.2_{-0.5}^{+0.2}$  keV, and an abundance of  $0.45_{-0.02}^{+0.03}$  solar, with a  $\chi^2/dof = 1.13$ . The *Chandra* data gave very poor constraints on the mass deposition rate or lower temperature with a  $\chi^2/dof = 0.87$  if  $kT_{\text{low}}$  was allowed to vary. From the f-test, the probability that the fit to the model with  $kT_{\text{low}}$  fixed is better than the fit with freeing  $kT_{\text{low}}$  is only  $2 \times 10^{-11}$  ( $9 \times 10^{-3}$ ) for the *XMM-Newton* (*Chandra*) data. For comparison, the mass deposition rate determined from *Einstein* data by surface brightness deprojection was  $\sim 53 M_{\odot} \text{ yr}^{-1}$  (White et al. 1997). As has been found in many other clusters (e.g., Peterson et al. 2003), the spectral data for Abell 2626 can be fit with significant amounts of gas cooling, but only by a factor of  $\sim 3$  in temperature.

#### 4.3. Density, Pressure and Entropy Profiles

Assuming the cluster is spherically symmetric, which appears to be roughly true for Abell 2626, the radial surface brightness profile (Figure 6) can be deprojected to give the X-ray emissivity  $\epsilon(r)$  and electron density  $n_e(r)$  as a function of radius (Appendix A). The electron density profiles determined from *XMM-Newton* and *Chandra* data are shown in the upper panel of Figure 11. Except for more fluctuations in the *Chandra* data, the two results for radii greater than  $\sim 7''$  are in good agreement. To avoid artifacts due to the assumption of zero emissivity outside the boundary during the deprojection (Takizawa et al. 2003), we have removed the 2 outermost points in each of the profiles plotted in Figure 11. In the *Chandra* data, we also note that the two innermost data points are higher than the *XMM-Newton* results by a factor of  $\sim 1.5 - 2$ . Such a deviation in the innermost data points can also be seen when comparing the surface brightness profile of *Chandra* data to *XMM-Newton* data (not shown in this paper). The surface brightness profile, as well as other profiles, is centered at the location of the southwest nucleus of the cD galaxy. The central deviation between *Chandra* and *XMM-Newton* might be due to the X-ray contribution of a central AGN (§ 4.7) and the differences in the PSFs of *XMM-Newton* and *Chandra*. The smaller PSF of *Chandra* allows the central excess to be resolved more readily. We did not remove the central source during the analysis, since it is probably extended in the 0.3–10 keV band (see § 4.7). Also, including or excluding this region does not change any other conclusions in the paper. The central excess extends to  $4'' - 7''$  in radius, which is larger than the PSF of *Chandra*. This probably indicates that the excess is not due to an AGN alone. The northeast nucleus of the cD galaxy is located at about  $4''$  away from the central AGN (Figure 3). From

the residual map (Figure 8), we clearly see that there is an extended excess around the northeast nucleus. There is also excess emission northwest of the AGN, which can also be seen in the soft band raw image of Figure 3.

The *XMM-Newton* data show that the electron density decreases from  $\sim 0.02 \text{ cm}^{-3}$  at  $\sim 7''$  to  $\sim 0.0004 \text{ cm}^{-3}$  at  $\sim 400''$ . The density profile is generally smooth, with a small jump around  $60''$  seen in the *Chandra* data. However, the jump is not visible with the *XMM-Newton* data. This radius corresponds to the location where the logarithmic slope of the surface brightness profile changes, or equivalently, to where the surface brightness goes from being dominated by the smaller to the larger of the two individual  $\beta$  models. We also noticed that the radio mini-halo is roughly confined within  $\sim 60''$ . Interestingly, this radius is also roughly coincident with the cooling radius (§ 4.4 below). Within the cooling radius and the region of the radio mini-halo, radiative cooling and/or the effects of the relativistic particles and magnetic fields in the radio plasma may affect the density profile of the X-ray gas.

The gas density and temperatures profiles can be combined to give the gas pressure  $P = nkT$ , where  $n$  is the total number density in the gas (both ions and electrons). We assume a fully ionized plasma with half cosmic abundances of heavy elements which gives  $n \approx 1.92 n_e$ . We also derive the gas entropy parameter  $S \equiv kT/n_e^{2/3}$  (Ponman et al. 2003). Since the spatial resolution of our density profile is much higher than the temperature profile, interpolation is used to determine the temperatures on the finer density grid by fitting a high order polynomial (lower panel of Figure 9). We assigned temperature errors of 5 (20)% at radii of smaller (larger) than  $250''$ . Using a constant temperature model gives similar results, except for more negative (unphysical) values for the total mass profile (§ 4.5 below). Thanks to the nearly constant temperature profile of Abell 2626, we believe that the interpolation of the temperature profile is reasonably accurate.

The pressure profile (middle panel of Figure 11) looks similar to the electron density profile, since the temperature is roughly constant. The feature at  $60''$  becomes more obvious, as the slope of temperature is negative in this region. At around  $240''$ , there is a slope change in the pressure profile. This is associated to the temperature jump at that radius, which may be a merger signature.

The entropy profile is shown in the lower panel of Figure 11. There is a small bump in the entropy profile around  $240''$  which is associated with the temperature jump and the change in slope of the pressure profile in the same region. The entropy may be boosted by a merger in that region. Excluding this entropy bump region, the logarithmic slope of the entropy profile in the outer regions ( $\sim 100'' - 400''$ ) is  $0.58 \pm 0.06$ , which is significantly smaller than the universal scaling relation slope of  $\sim 1.1$  (e.g., Ponman et al. 2003). Note that there is a large scatter in the entropy profiles of individual clusters (e.g., Figure 1, Ponman et al. 2003), and hence the smaller logarithmic slope might not be unusual. There is a difference in the central entropy measured by *XMM-Newton* and *Chandra*. This central entropy deviation comes from the difference in central gas density measurements, which



is probably due to the combination of a central excess in X-ray emission and differences in the PSFs of *Chandra* and *XMM-Newton*. However, the spatial resolutions of the temperature measurements are not sufficient to determine if the entropy differences are due to the temperature in the hot gas, or a central X-ray source. In the following, we chose to present results of the *XMM-Newton* data with which the spatial resolution in density profile measurement is poorer. The *XMM-Newton* data show that the entropy decreases from the outer value of  $\sim 360 \text{ keV cm}^2$ , eventually flattening to a value of  $\sim 30 \text{ keV cm}^2$ . If there is no feedback mechanism, a pure radiative cooling model will result in a power law entropy profile, with central entropy lower than  $\sim 10 \text{ keV cm}^2$  within 10 kpc (Figure 1 of Voit & Donahue 2005). The central entropy pedestal value of  $\sim 30 \text{ keV cm}^2$  implies that there has to be heating in the central region, which can probably be explained by a central AGN.

#### 4.4. Cooling and Thermal Conduction Time Scales

Three important processes, heating, cooling and heat conduction, determine the thermal structure in the hot gas (e.g., Sarazin 1986). While the heating process in the central region is probably due to the AGN, the other processes are related to the hot gas structure itself. Here we compare two important time scales for the hot gas - the cooling and thermal conduction time scales. For the temperature gradients seen in typical cooling flow clusters, conduction is likely to be an important process if it is not suppressed by the magnetic field.

The cooling time was determined for each radius in the deprojected density profile using the values of the deprojected density and the deprojected temperature for both *XMM-Newton* and *Chandra* data. The rate of total emission from the gas was determined using the same MEKAL model used to fit the spectra. The integrated, isobaric cooling time  $t_{\text{cool}}$  was determined. A brief outline of the cooling time estimation procedure is given in Appendix B.

We define the conduction time scale to be (Sarazin 1986)

$$t_{\text{cond}} \equiv \frac{n_e(T/|\nabla T|)^2 k}{\kappa}, \quad (2)$$

where  $\kappa$  is the thermal conductivity for a hydrogen plasma (Spitzer 1962),

$$\kappa = 4.6 \times 10^{13} \left( \frac{T}{10^8 \text{ K}} \right)^{5/2} \left( \frac{\ln \Lambda}{40} \right)^{-1} \text{ ergs s}^{-1} \text{ cm}^{-1} \text{ K}^{-1}, \quad (3)$$

and  $\Lambda = 37.8 + \ln[(T/10^8 \text{ K})(n_e/10^{-3} \text{ cm}^{-3})^{-1/2}]$  is the Coulomb logarithm.

Figure 12 shows the cooling and conduction time scales as a function of angular radius. The cooling time scale (plus symbols) decreases from  $\sim 50 \text{ Gyr}$  at  $\sim 540''$ , down to  $\sim 1 \text{ Gyr}$  at  $\lesssim 15''$ . Assuming the cluster has not changed much since  $z \sim 1$ , we define the cooling radius to be where  $t_{\text{cool}}$  is equal to the time since  $z = 1$ , which is 7.7 Gyr. The cooling radius,  $r_{\text{cool}}$ , is thus  $\sim 60'' - 70''$  ( $\sim 66 - 77 \text{ kpc}$ ). Interestingly,  $r_{\text{cool}}$  is of the same size as the mini-halo (see § 3.4). It is also located near the radius where the logarithmic slope of the surface brightness profile changes, or equivalently, where the surface bright-

ness profile goes from being dominated by the smaller to the larger of the two individual  $\beta$  models (§ 3.3).

The conduction timescale depends on the temperature gradient, which is strongly affected by the uncertainties in the individual temperature points. The error estimation for the conduction timescale is complicated by the fact that the adjoining deprojected temperatures used to derive the conduction timescale are correlated. Hence, in calculating the uncertainties by error propagation, we included the full covariance matrix for the temperatures obtained from the deprojection using XSPEC. In the upper panel of Figure 12, the crosses show the values of the conduction time derived using the individual temperature values derived from annular *XMM-Newton* spectra (§ 4.1). The conduction time derived from the *Chandra* data (lower panel of Figure 12) are in general shorter than those from the *XMM-Newton* data. This may be due to the much larger scattering of the *Chandra* deprojected temperature profile. The error bars of the *Chandra* data are much larger than that of the *XMM-Newton* data. In order to reduce the effects of the uncertainties of the *Chandra* data, we also determine the conduction time scale in the inner region using the same interpolated temperature profile which was used to deproject the pressure/entropy profile (§ 4.3). The interpolated temperature profile was also used for the *XMM-Newton* data for comparison. These values are shown as dots in Figure 12; the upper panel gives the values for the *XMM-Newton* data, and the lower panel is for the *Chandra* data. The *Chandra* conduction time scales are longer than the *XMM-Newton* values in the innermost regions due to the higher densities derived there from the *Chandra* data.

Here we describe results obtained from *XMM-Newton* since the error bars are much smaller than those from *Chandra*. In the central regions of Abell 2626, the temperature gradient is very flat. The overall temperature variation is only about 0.4 keV within the cooling radius of  $\sim 65''$ . Both the best-estimate and the lower bound on the conduction time are larger than the cooling time in the central regions of the cluster. The nearly isothermal temperature profile in Abell 2626 and resulting low conduction imply that thermal conduction is not important compared to cooling anywhere the cooling rate is high. Hence, in Abell 2626 the thermal structure within the cooling radius of  $\sim 65''$  is probably determined by cooling and heating processes only. At a radius of  $\sim 240''$ , the conduction time scale drops to  $\sim 0.3 \text{ Gyr}$  only, which is significantly shorter than the look-back time to a redshift  $z \sim 1$ . Even including the uncertainty in the conduction timescale, the upper limit on the time scale is still quite short. This indicates that either the thermal structure (perhaps associated with a merger) happened within  $\sim 0.3 \text{ Gyr}$ , or thermal conduction is suppressed at least by a factor of  $\sim 20$ . Except the feature at  $\sim 240''$ , outside of  $\sim 65''$ , we cannot determine whether thermal conduction is important or not due to the large uncertainties.

#### 4.5. Mass Profiles

Figure 13 shows the gas mass and total mass profiles of Abell 2626. The gas mass profile is given by

$$M_{\text{gas}}(< r) = \int_0^r 4\pi(r')^2 dr' \rho_{\text{gas}}(r'), \quad (4)$$

where  $\rho_{\text{gas}} = \mu_e n_e$  is the gas mass density, and  $\mu_e$  is the mass per electron determined from the gas abundances.

The total mass of the cluster can also be determined if we assume the hot gas is in hydrostatic equilibrium, and if the temperature of the hot gas is known. The total mass profile is given by (e.g., Sarazin 1986):

$$M_{\text{tot}}(< r) = -\frac{kTr}{\mu m_p G} \left( \frac{d \ln \rho_{\text{gas}}}{d \ln r} + \frac{d \ln T}{d \ln r} \right), \quad (5)$$

where  $\mu$  is the mean mass per particle, and  $m_p$  is the proton mass. The temperature profile was interpolated from the *XMM-Newton* data (Figure 9, § 4.3). Since the mass within any given radius is determined by local gas properties and their derivatives, the total mass can decrease or can even be negative. (This occurred at  $r = 57''$  for *XMM-Newton* and at a number of points for *Chandra*, and these points were omitted from the plot.) This can be due to measurement uncertainties in the data, which are compounded by the derivatives, or by the breakdown of simple hydrostatic equilibrium. The radio mini-halo is within  $\sim 60''$ , and may be disturbing the hot gas or contributing additional pressure support in this region (§§ 3.1.2 & 3.4). Thus, the mass profile at small radii may not be represented accurately by hydrostatic equilibrium. At radii of  $r \gtrsim 60''$ , the general trend is for  $M(< r)$  to increase with radius.

Compared to White et al. (1997) rescaled to our value of the Hubble constant, the gas masses we have obtained agree to within 2% and 7% at  $321''$  and  $489''$ , respectively. The total mass agrees within 26% at  $321''$ . The difference in the total mass at this radius is large, but the values still agree within the uncertainties. The two values of the total mass do not agree at  $489''$ , probably due to the larger uncertainty in the temperature in the outermost annulus. The gas mass fraction ( $M_{\text{gas}}/M_{\text{tot}}$ ) increases from  $\sim 5\%$  at  $100''$  to  $\sim 10\%$  at  $500''$ . The global trend is the same as is typical in relaxed clusters (David et al. 1995; Ettori & Fabian 1999; Allen et al. 2002).

#### 4.6. Hardness Ratio Maps

To understand the rough spectral properties of different regions, we have created hardness ratio maps from both *XMM-Newton* and *Chandra* data (Figures 14, 15, & 16). For *XMM-Newton* data, the PN image was not included because of its different spectral response and because the chip gaps and bad columns produced cosmetic artifacts in the smoothed image. The hardness ratio maps were created by dividing the image in the hard band (2–10 keV) by the image in the soft band (0.3–2 keV). Each image was background-subtracted, exposure-corrected, and smoothed with the same scales as the  $3\sigma$  adaptively smoothed image of the 0.3–10 keV band. We also tried smoothing all images with the same scales as the  $5\sigma$  adaptively smoothed image of the 0.3–10 keV band, or with the same scales as the  $3\sigma$  adaptively smoothed image of the hard band (2–10 keV), and almost all the features look the same as the hardness ratio maps given in this paper. While some features are not consistently seen in both the *XMM-Newton* and *Chandra* hardness ratio maps, indicating the possibility that they are statistic fluctuations in at least one of these maps, the common features which show up in both maps in

the inner regions should be real (Figure 15). The colors from black to blue to red to yellow to white represent the degree of hardness from soft to hard. Though the hardness ratio maps from *XMM-Newton* and *Chandra* cannot be directly compared due to different spectral responses, the relative hardness is still useful to identify interesting regions.

##### 4.6.1. Global Structure

Figure 14 is the hardness ratio map of the whole Abell 2626 from *XMM-Newton* data, overlaid with green contours of excess emission from the *XMM-Newton* residual map (left panel of Figure 7). Part of the apparent inhomogeneity in hardness is just due to noise. Also, near the blue and dark boundary of the hardness ratio map, the features start to be dominated by the hard background. Although difficult to see due to the rather flat temperature profile, the overall picture is a soft core at the center. At larger radii, the hardness increases outward to a radius indicated around the central cyan (light blue) circle, and then the hardness decreases outward. The central cyan circle is at a radius of  $240''$  where the jump in temperature was identified (§ 4.1). From the hardness ratio map, it seems that the harder gas is confined within the cyan circle.

The white circles in Figure 14 are the two extended X-ray emission regions associated with the merging subclusters (§ 3.1.1). The discontinuities in the green contours near the white circles are actually artifacts of chip gaps. Both of the extended X-ray emission regions appear to be harder than their surroundings, and each of them contains a softer point-like source. The soft source in the northeast extended X-ray emission region is located at the peak of the extended emission, and is probably associated with the galaxy 2MASX J23365372+2113322 (Table 1), while the soft source in the southwest region is not associated with any identified galaxy. The two soft point-like sources in the two extended emission regions disappeared when the images were smoothed with the same scales as the  $5\sigma$  adaptively smoothed image of the 0.3–10 keV band, or with the same scales as the  $3\sigma$  adaptively smoothed image of the hard band (2–10 keV).

##### 4.6.2. Central Region

The details of the central region of the hardness ratio maps are shown in Figure 15. Contours of excess emission are shown from the *Chandra* residual map (right panel of Figure 7). While the *XMM-Newton* and *Chandra* hardness ratio maps do not agree completely, probably due in part to noise and in part to the larger PSF of *XMM-Newton*, we can still identify some common features.

One interesting feature is that the S0 galaxy IC 5337 shows a softer tail in the western direction. On the *Chandra* hardness ratio map (right panel of Figure 15), there is a narrow tail of soft emission starting from the southern corner of the IC 5337 tail and extending to the SWW. We also see a softer region with a similar scale in the *XMM-Newton* hardness ratio map (left panel of Figure 15).

The northern excess region  $\sim 30''$  above the cD galaxy (contours) appears softer, with an extension towards the northeast direction which can also be seen in Figure 14. If the region is near hydrostatic equilibrium and the material is supported by ideal gas pressure, we would expect

the brighter (and hence denser) regions to have softer spectra. This is roughly the case for the northern excess region. However, for the southern excess at a similar radius where the tongue is located (§ 3.1.2), the brighter excess region does not correspond to a softer region, which suggests a breakdown of hydrostatic equilibrium. In particular, the X-ray excess tongue in the south direction of the cD galaxy (compared to Figure 8) appears to overlap both hard and soft regions extending in the same direction, making it hard to understand its origin.

Between the main cluster and the southwest subcluster, the large extended region of excess emission near the southwest corner appears to have a harder spectrum in the *Chandra* data (right panel of Figure 15), while it appears to be soft in the *XMM-Newton* data (left panel of Figure 15). From the hardness ratio map, it is not clear whether the extended excess is a shock heated region or a cold front.

In Figure 16, we can see clearly that there are two hard point sources located at the position of the cD galaxy IC 5338 and the S0 galaxy IC5337 (arrows). The interpretation of two AGNs will be discussed in § 4.7. Radio contours (Gitti et al. 2004) are overlaid on the *Chandra* hardness ratio map to show in detail the complicated thermal and radio structures in the central region. The southern radio bar appears to be in a harder region, while the northern one appears softer. If the radio bars are indeed thin tubes along the plane of the sky, the X-ray emission along the line-of-sights may mainly be contributed by the cluster emission beyond the central region. In this case, the projected image or hardness ratio would not necessarily reflect the X-ray emissivities or hardnesses of the radio bars, and hence the lack of symmetry or a clear correspondence with features in the X-ray images or hardness maps might be understandable.

#### 4.7. Possible X-ray AGNs in IC 5338 and IC 5337

We searched for evidence of a central point source associated with the cD galaxy IC 5338, which may indicate the existence of an X-ray AGN. When *wavedetect* was run on the 0.3–10 keV and 0.3–2 keV band *Chandra* images (§ 3.2), each detected one central source located at the southwest and northeast nucleus of the cD galaxy, respectively. Both were possibly extended. We also ran *wavedetect* on the hard band (2–10 keV) image, but it did not detect a central point source. However, when we inspected the hard band image, we noticed a possible hard point source. This source can be seen in the *Chandra* hardness ratio map (Figure 16). We extracted the *HST* image of the center of IC 5338 from the archive. The 300 s exposure was taken on 1999 June 26 using the *HST* WFPC2 camera with the F555W filter. Figure 3 shows clearly that this cD galaxy has two distinct nuclei, with the northeast nucleus being brighter optically. The two optical nuclei are located at the peaks of the soft X-ray image, with the radio core source in IC 5338 centered on the hard X-ray, southwest nucleus. The hard X-ray point source is only separated from the peak of the radio core by less than 1". Thus, we believe that this source is the AGN, and that the point-like hard X-ray source arises from this AGN.

To study the X-ray properties of the IC 5338 AGN, *Chandra* data were used to do photometry. Due to the limited number of photons, we cannot fit the spectrum

of the AGN. Hence, we estimated the properties of the cD AGN by assuming that it has a power law spectrum with a photon index  $\Gamma$ . We extracted the total photon counts in a circular region with a 3 pixel radius in both hard (2–10 keV) and soft (0.3–2 keV) bands. In order to subtract the cluster emission as well as true background, we took background from a 3-pixel-wide annulus just outside the central region. The program *PIMMS*<sup>6</sup> was used to determine the photon index and the unabsorbed flux which gave the correct hardness ratio and photon counts. We assumed that absorbing column was given by the Galactic value  $N_H = 4.2 \times 10^{20} \text{ cm}^{-2}$  (Dickey & Lockman 1990). The best fit photon index is  $\Gamma = 2.2^{+0.7}_{-0.4}$ . The unabsorbed flux in the 0.3–10.0 keV band is  $F_X = 1.6^{+0.7}_{-0.4} \times 10^{-14} \text{ ergs cm}^{-2} \text{ s}^{-1}$ , which gives an X-ray luminosity of  $L_X = 1.2^{+0.5}_{-0.3} \times 10^{41} \text{ ergs s}^{-1}$  in the same energy band.

We also searched for evidence for a point source associated with an AGN in the center of the X-ray bright S0 galaxy IC 5337. In this case, *wavedetect* did detect a point source in the *Chandra* hard band (2–10 keV) image at the center of IC 5337. This point-like, hard source is clearly seen in the hardness ratio map (Figure 16). The S0 galaxy is also a radio source, and the X-ray point source is apparently associated with this central AGN. Again, the point source was too faint for spectral fitting. Using the same method described above, we determined the best-fit spectral index and flux assuming the Galactic hydrogen column density of  $4.2 \times 10^{20} \text{ cm}^{-2}$ . The best fit photon index is  $\Gamma = 0.2^{+0.6}_{-0.3}$ , the unabsorbed flux in the 0.3–10.0 keV band is  $F_X = 3.2^{+1.9}_{-1.7} \times 10^{-14} \text{ ergs cm}^{-2} \text{ s}^{-1}$ , and the X-ray luminosity is  $L_X = 2.4^{+1.5}_{-1.3} \times 10^{41} \text{ ergs s}^{-1}$ . This spectrum index seems to be low (hard) for a typical AGN. One possibility is that there is excess internal absorption associated with the S0 galaxy AGN. To assess this, we fixed the photon index to  $\Gamma = 1.5$ . In this case, the best-fit hydrogen column density is  $N_H = 1.3^{+0.7}_{-0.8} \times 10^{22} \text{ cm}^{-2}$ , the unabsorbed flux is  $F_X = (3.0 \pm 1.5) \times 10^{-14} \text{ ergs cm}^{-2} \text{ s}^{-1}$ , and the X-ray luminosity is  $L_X = (2.3 \pm 1.1) \times 10^{41} \text{ ergs s}^{-1}$ . Somewhat counterintuitively, the extra absorption gives a lower unabsorbed flux because of the steeper spectral index assumed.

#### 5. KINEMATICS OF THE S0 GALAXY IC 5337

The bow-shock-like shape suggests that the S0 galaxy is moving east directly towards the cluster center (right panel of Figure 2). The hardness ratio maps of the center of the cluster (Figures 15 & 16) show a region of soft (and presumably, cool) X-ray emission extending to the west of the S0 galaxy. This geometry would be consistent with the S0 galaxy falling into the cluster from the west; the cool tail of gas would be either interstellar or intragroup gas associated with this galaxy which is being stripped by ram pressure from the motion through the ICM of Abell 2626. The steepness of the intensity gradient in the cluster radio mini-halo on the western side compared to the eastern side (left panel of Figure 2) may also indicate that it is compressed by the S0 galaxy.

The radio structure complicates the interpretation of

<sup>6</sup> <http://heasarc.gsfc.nasa.gov/Tools/w3pimms.html>

the motion of the galaxy, since there is a component centered on the S0 galaxy, and a component located at a position of about  $190^\circ$  (measured from north to east) of the S0 galaxy on the 1.5 GHz B-array map (Figures 2, 8, & 16). The 1.5 GHz C-array map shows three radio tails in the south, southwest and west directions. If the south component is a Narrow-Angle-Tail (NAT) behind the S0 galaxy, then it is likely to be moving to the NNE (about  $10^\circ$  measured from north to east) direction. On the other hand, the other two components (west and southwest tails) are more consistent with the bow-shocked structure in the X-ray image which indicates that the S0 galaxy is moving to the east.

The interpretation of the kinematics of IC 5337 is confused by an ambiguity in the literature concerning its radial velocity. There are two optical determinations of the radial velocity which give values which are consistent with the velocity of other galaxies in the center of Abell 2626, including the cD galaxy IC 5338. Huchra et al. (1999) give a velocity of  $16,485 \pm 37 \text{ km s}^{-1}$ , and Falco et al. (1999) find  $16,562 \pm 60 \text{ km s}^{-1}$ . These values are consistent with the 21 cm line determination of  $16,485 \pm 40 \text{ km s}^{-1}$  by Giovanelli & Haynes (1993). On the other hand, Mohr et al. (1996) list an optical velocity of  $18,903 \pm 39 \text{ km s}^{-1}$ , and Karachentsev & Kopylov (1981) list a velocity of  $19,097 \text{ km s}^{-1}$  with an uncertainty of the order of  $100 \text{ km s}^{-1}$ . The difference between these velocities and the others is much greater than the quoted (or any likely) measurement errors. The velocities given by Mohr et al. (1996) and Karachentsev & Kopylov (1981) would be inconsistent with IC 5337 being a part of the main central cluster Abell 2626. On the other hand, these higher velocities are consistent with IC 5337 being a member of the southern subcluster with a mean velocity of  $19,164 \pm 138 \text{ km s}^{-1}$  (Mohr et al. 1996). Most of the other members of this subcluster lie considerably to the south.

If IC 5337 is a member of the southern subcluster, its dynamics would probably follow somewhat the motion of the subcluster. We would expect IC 5337 would be infalling from SSW to NNE (towards the position angle of  $30^\circ$  direction measured from north to east). This would be inconsistent with our interpretation of the bow-shaped X-ray region to the east of IC 5337. Based on the X-ray image, we suggest that IC 5337 is falling directly into the main cluster from the west, and may not be associated with the southern subcluster. On the other hand, given that there are two velocity measurements consistent with the kinematics of the southwest subcluster (Mohr et al. 1996; Karachentsev & Kopylov 1981), it seems unlikely that both are in error in the same way. One possible explanation is that there are two galaxies located along the line-of-sight toward IC 5337. Indeed, on the *Chandra* X-ray image, there are two point sources identified within the extended optical emission of IC 5337. One is located at the center of the S0 galaxy with two west and southwest NATs, while the other is located at its southern edge with a south NAT. The southern X-ray source was removed during the analysis related to the S0 galaxy in this paper. We have accessed the public available IR<sup>7</sup>, optical<sup>8</sup> and UV<sup>9</sup> surveys to search for a point source at

the location of the southern X-ray point source. While there is no obvious emission in the IR H and K band images, there seems to be extended emission associated with the southern X-ray source in the IR J band, optical band and the UV band images. However, one cannot easily determine if this emission is a separate galaxy or a feature in the disk of the S0 galaxy.

## 6. COOLING FLOW INTERACTION WITH THE CENTRAL RADIO SOURCE?

The most unusual features of the radio image of Abell 2626 are the two elongated radio bars to the north and south of the radio core (Figures 2, 8, & 16). Their symmetric positions suggests they are radio lobes, but their elongated shapes are unusual. By comparison to radio lobes associated with other cooling core dominant radio galaxies, one might expect these to be regions of reduced X-ray emission surrounded by bright rims (“radio bubbles”, Fabian et al. 2000; Blanton et al. 2001). In radio bubbles, the radio plasma has apparently displaced the X-ray gas. One would expect the level of reduction in the X-ray surface brightness to depend on the extent of the bubbles along the line-of-sight. If they are highly oblate flattened regions with a large extent along the line-of-sight, the reduction in the X-ray surface brightness might be quite significant. If they are highly prolate tubes, then the reduction would be small. In fact, there is no obvious correlation between the two radio bars and the *Chandra* X-ray image, residual map or hardness ratio map in Figures 2, 8, & 16, respectively. This may indicate that the radio bars are thin tubes, with a small extent along the line-of-sight, or that the radio plasma is mixed with the X-ray gas. In the numerical simulations by Robinson et al. (2004), if the magnetic field of the bubble is weak, the bubble is very unstable and can be destroyed easily, leaving no obvious density contrast. The ratio of gas to magnetic pressure in the center of Abell 2626 is of the order of 100 (Rizza et al. 2000; Gitti et al. 2004), which is the same order as the weak magnetic field in the simulation by Robinson et al. (2004). However, it should be noted that the magnetic field in the radio bars could be much higher. One concern with this model is that it seems unlikely that such mixing would preserve the narrow radio bars which are observed.

One possible interpretation of the arc-like X-ray feature near the center of Abell 2626 (upper right panel of Figure 3) is that the central cD galaxy is moving to the west relative to the local intracluster gas. This could explain the bending of the X-ray emission near the center and the inner radio jets, as well as the elongation of the radio bars. However, in this case one might expect that the western edges of the two radio bars would indicate the positions where the radio jets have stopped. These positions are not mirror symmetric about the position of the radio core, as might be expected for jets perpendicular to the motion of the nucleus of the cD galaxy. Even if the jets are not perpendicular to the motion of the nucleus, one of the western edges of the two radio bars should have been behind the nucleus of the cD galaxy in this interpretation.

<sup>7</sup> 2MASS: <http://irsa.ipac.caltech.edu/Missions/2mass.html>

<sup>8</sup> The STScI Digitized Sky Survey:

[http://stdu.stsci.edu/cgi-bin/dss\\_form](http://stdu.stsci.edu/cgi-bin/dss_form)

<sup>9</sup> GALEX: <http://www.galex.caltech.edu/>

There are two X-ray excess “tongues” from the central cD galaxy to the two radio bars, with the southern “tongue” appears to be stronger (upper right panel of Figure 3, & Figure 8). A similar tongue has been seen in Abell 133, where it was suggested that it might arise from a cluster merger, Kelvin-Helmholtz instabilities around the core, the buoyant uplift from a radio bubble, or a cooling wake (Fujita et al. 2004). Although subclusters may be merging with the outer regions of Abell 2626, there is no clear evidence for merger distortion in the central region. Even though the two cD nuclei may indicate a previous merger, the two nuclei are well inside the cD galaxy, which means that any associated merger may have happened a long time ago. Also, a merger might be expected to produce a tongue and radio lobe on only one side of the nucleus, as in Abell 133. For Abell 2626, the mean line-of-sight velocity of the galaxies is  $16,533 \text{ km s}^{-1}$ , while that of the central cD galaxy is  $16,562 \text{ km s}^{-1}$  (Mohr et al. 1996), so the radial velocity of the cD galaxy relative to the cluster is low. Moreover, there is no obvious cold or shock front, which means that any motion in the plane of the sky is also slow. Therefore, there is no obvious velocity for the cD galaxy to induce Kelvin-Helmholtz instabilities. If the tongue is caused by a cooling wake, there would be only one. But we see two of them, though the northern one is much weaker than the southern one.

Eliminating the explanations by a cluster merger, Kelvin-Helmholtz instabilities and the cooling wake, the tongue seems to be best explained by the buoyant uplift from a radio bubble. In fact, a recent simulation indicates that when a bubble rises in the intracluster medium, large rolls extend out and converge under the bubble. This results in an upwelling and compression of material under the wake of the bubble (Robinson et al. 2004). The morphology of the southern tongue shown in Figure 8 looks very similar to the simulated result (Robinson et al. 2004) if we assume that the radio bar is the head of the plume. However, if the southern “tongue” is caused by uplifted cool gas, why is the northern X-ray tongue associated with the northern radio bar much weaker, given the two radio bars are similar in appearance? While there is no radio flux measurement to the radio bars in the literature, the stronger of the radio emission from the southern bar can be noted on the VLA 330 MHz B+DnC-array radio map of Figure 4 in Gitti et al. (2004). This may explain the stronger uplift of the thermal plasma in the south.

Jet precession might also provide a natural explanation of the structure of the central region. The southwest cD nucleus is an AGN (see § 4.7), and may be ejecting two jets towards the north and south. We assume the two jets are precessing about an axis which is nearly perpendicular to the line-of-sight along the north-south direction, so that the jets sweep out two conic surfaces to the north and south. If the two jets are stopped at approximately equal radii from the AGN (at a “working surface”), and if radio emission is produced by particles accelerated when the jets are stopped, then the radio bars might be produced as the jets precessed. If the jets are narrow, then the radio emission at the working surface may be narrow, explaining the shape of the radio bars and also the lack of anticorrelation between the two radio bars and the X-ray emission. The preces-

sion of the jets might be due to the gravitational effects of the second cD nucleus to the north, and this nucleus might have disrupted or weakened the northern X-ray tongue. Alternatively, the dominance of the southern X-ray tongue may simply be due to the southern jet being more powerful. There is also evidence of jet precession in other cooling core clusters (Gitti et al. 2006). Jet precession has also been suggested to be a requirement for the AGN feedback mechanism to solve the cooling flow problem (Vernaleo & Reynolds 2006).

Abell 2626 is one of the clusters associated with a possible radio mini-halo, an extended diffuse radio source in the cooling core region of the intracluster medium (Gitti et al. 2004). In the cooling core region, the magnetic field strength is expected to be high due to compression. Consequently the radiative cooling time of the relativistic electrons is expected to be as short as  $\sim 10^7 - 10^8 \text{ yr}$ , which is much shorter than the time needed to travel across the extended region (Gitti et al. 2004). In order to explain the existence of the radio mini-halo, an *in-situ* re-acceleration mechanism is needed. The steep radio spectrum of the mini-halo ( $\alpha \sim 2.4$ , Gitti et al. 2004) may be due to confinement by the X-ray gas and radiative losses by the relativistic electrons.

While there is no very obvious correlation between the radio emission from the mini-halo and the X-ray emission from the X-ray images (Figure 2), there is some evidence of interaction between the radio mini-halo and the surrounding intracluster medium in the residual maps (Figure 8). In general, the diamond-shaped outline of the extended radio emission (the radio “mini-halo”) corresponds to a region of reduced X-ray emission, and there are excess X-ray regions NNE and SSW of the edge of the mini-halo where the radio surface brightness is dropping rapidly. The mini-halo is roughly confined within  $60''$ . The distance from the center to the NE or SW corners of the diamond is about  $50''$ ; while to the NW or SE corners is about  $70''$ . As noted previously (§ 3.4), in the interpretation of Gitti et al. (2004) the two radio bars are distinct from the diffuse radio emission, and in fact after their subtraction the morphology of the mini-halo become roughly circular (see Figure 6 of Gitti et al. 2004), though we can still see some excess radio emission in the NW and SE corners. Interestingly, there is also a small density jump in the X-ray gas around  $60''$  (§ 4.3 above). The size of the mini-halo is also coincident with the cooling radius (§ 4.4 above). This supports the re-acceleration model for the origin of the mini-halo (Gitti et al. 2004), though it could just be a coincidence since the definition of the cooling radius is somewhat arbitrary.

An excess in the residual map corresponds to a region where the gas density is higher than in the symmetric model (Figure 8). The shape of the mini-halo, if it is really elongated in shape (after proper subtraction of the radio bars), may be due to variations in the X-ray gas density. The radio source may be more strongly confined by the gas in the NE and SW directions. The points on the diamond-shaped radio mini-halo to the NW and SE may indicate regions of lower gas density where the radio plasma has been able to expand more. On the western side of the radio mini-halo, the intensity gradient is steeper than that of the eastern side. This may be due to gas compression by the S0 galaxy IC 5337 falling to

wards the cD galaxy IC 5338. If this is the case, then IC 5337 should be very close to the central cooling core, rather than being part of the southwest subcluster. This reinforces both our dynamical picture for the S0 galaxy and the interpretation of the mini-halo geometry by confinement. The X-ray deficient regions in the NW and SE directions can also be seen on *XMM-Newton* residual map on a larger scale (dark regions of the left panel of Figure 7). The excess of intracluster gas density to the NE and SW might be due to mergers along the axis of the local large scale structure, as discussed in § 3.1.1, or it may just represent the elongation of the equilibrium distribution of the gas in this direction. The lower density regions in the NE and SW directions can also be regions inflated by previous radio bubbles. Although the symmetric radio bars may be due to the jet precession, it is also possible that the denser gas to the NE and SW might explain the shape of the two radio bars; the radio bars might have been compressed radially by a collision with this gas, and become extended to the NW and SE by the smaller ICM density gradients in those directions.

## 7. CONCLUSIONS

We have identified two extended X-ray emitting regions about  $7'$  northeast and southwest from the center of Abell 2626, with the latter one probably associated with a subcluster identified to be falling into the main cluster (Mohr et al. 1996; Mohr & Wegner 1997). We argue that the infalling velocity of the southwest subcluster is mainly along the line-of-sight. Abell 2626 is known to be associated with the Perseus-Pegasus supercluster (Batuski & Burns 1985a,b; Zucca et al. 1993; Einasto et al. 2001), and it is likely that the main cluster is accreting subclusters and groups from this large-scale structure (§§ 3.1.1, 3.4, & 4.6.2). From the hardness ratio map, both of the extended X-ray emitting regions appear to be harder than their surroundings, and each of them contains a softer point-like source. The northeast point-like source may be associated with the galaxy 2MASX J23365372+2113322.

Based on the bow shape of the X-ray emission and the soft X-ray tail identified by the hardness ratio map, we argue that the S0 galaxy IC 5337 is falling towards the center of the main cluster from the west. The steeper intensity gradient in the cluster radio mini-halo on the western side compared to the eastern side may also indicate that the radio plasma is compressed by the S0 galaxy. This reinforces our interpretation that the S0 galaxy should be close to the cooling core region instead of located inside the southwest subcluster. On the other hand, if the S0 galaxy were associated with the subcluster in the southwest direction, this motion would be hard to understand. While there are two velocity measurements of IC 5337 consistent with the southwest subcluster and three measurements consistent with the main cluster, one possible explanation is that there may be two galaxies along the line-of-sight of IC 5337.

We have identified hard X-ray point sources due to AGNs associated with the cD galaxy IC 5338 and the S0 galaxy IC 5337, both of which are radio sources. The cD galaxy AGN is located on the southwest nucleus of the cD galaxy. The S0 galaxy AGN shows evidence for excess internal absorption.

We have used a double beta model to fit the radial sur-

face brightness profile and generated residual images to understand the dynamics of the intracluster gas (§ 3.4). Most of the residual structures in the inner region occur on a scale similar to that of the radio sources in the center. One major residual in the inner cluster which is not on the scale of the radio emission is the extended excess to the southwest. It is located between the cD galaxies and the southwest subcluster, and may be the result of a merger.

The gas temperature in Abell 2626 increases from a central value of  $\sim 2.5$  keV at  $\sim 10$  kpc to a maximum of  $\sim 3.5$  keV at around 230 kpc, and then decreases to  $\sim 1.5$  keV at  $\sim 600$  kpc. At a radius of  $\sim 260$  kpc, there is a significant temperature jump seen in the fits to the *XMM-Newton* spectra. The jump may be associated with a previous or an ongoing merger. We used the X-ray spectra to determine the cooling rate within a projected radius of 72 kpc. The amount of gas which is cooling down to very low temperatures is less than a few  $M_{\odot} \text{ yr}^{-1}$ . A much higher mass deposition rate of  $\sim 74 M_{\odot} \text{ yr}^{-1}$  is obtained from the *XMM-Newton* spectra if the hot gas only cools by about a factor of three.

From the surface brightness and the temperature profiles, we have derived the density, pressure, and entropy profiles of Abell 2626. At a radius of  $\sim 70$  kpc, there is a slope discontinuity in the density and pressure profiles. The outer entropy profile has a logarithmic slope of  $\sim 0.58$ , which is lower than that of the universal scaling relation of  $\sim 1.1$ . A heating source is probably required to maintain the central entropy of  $\sim 30 \text{ keV cm}^2$ . At a radius of  $\sim 260$  kpc, there is a small bump in the entropy profile which may be associated with a merger.

Due to the nearly isothermal structure of Abell 2626 within the cooling radius, conduction is not important compared to cooling in the inner region. The cooling radius is  $\sim 70$  kpc, where the logarithmic slope of the surface brightness profile changes. At a radius of  $\sim 260$  kpc, the conduction time scale is significantly shorter than the look-back time to a redshift of  $z \sim 1$ , which indicates that either the thermal structure (perhaps associated with a merger) happened recently or thermal conduction is highly suppressed. We have also derived the total mass profile under the assumption of hydrostatic equilibrium, and compared the gas mass fraction with other relaxed clusters. The global trend is typical for relaxed clusters.

We have investigated the cooling flow interaction with the central radio source. The two elongated radio bars to the north and south of the center of the cD galaxy and the lack of obvious correlation between the two radio bars and any structures in the *Chandra* X-ray image, residual image, or hardness ratio map may indicate that the radio bars are thin tubes parallel to the plane of the sky. Another possibility is that the radio plasma is mixed with the X-ray gas, rather than displacing it.

The central radio structure may be due to jet precession. The southwest cD nucleus is an AGN, and we suggest it has two precessing jets propagating towards the north and south, producing the two symmetric narrow radio bars. The precession might be caused by the gravitational influence of the second cD nucleus to the north. The two jets may have uplifted cool gas from the central region, producing the X-ray excess ‘‘tongues’’ running from the center of the cD galaxy to the radio bars. The northern tongue appears to be weaker, and it may

be disrupted by the northern nucleus of the cD galaxy. Alternatively, the strength of the southern X-ray tongue may simply be due to the southern jet being stronger. Jet precession may also be found in other cooling core clusters (Gitti et al. 2006). It may help to solve the AGN feedback problem found in high resolution simulations (Vernaleo & Reynolds 2006). Alternatively, the distortions of the radio source might be due to ICM motion, particularly rotation, near the center of the cluster.

The radio mini-halo has a diamond shape, elongated in the northwest and southeast direction. The diamond-shaped radio mini-halo seems to be compressed from the northeast and southwest direction, which is probably consistent with the merging scenario for Abell 2626. With this compression geometry, the radio mini-halo might be leaking out in the northwest and southeast direction (Figure 8). The western side of the mini-halo may also be compressed by the infalling S0 galaxy IC 5337. Interestingly, the size of the mini-halo is roughly the same as the cooling radius, and is located at where the logarithmic slope of the surface brightness profile changes. The agreement between the size of the radio mini-halo and the cooling radius is consistent with the re-acceleration model for the origin of the mini-halo (Gitti et al. 2004), although it might just be a coinci-

dence since the definition of the cooling radius is somewhat arbitrary. Independent of the origin of the radio mini-halo, the change in the X-ray surface brightness slope at the outer edge of the radio mini-halo may indicate that the radio plasma is affecting the thermal plasma.

We would like to thank H. Andernach, M. N. Chatzikos, T. E. Clarke, M. Gitti, A. M. Juett, J. J. Mohr, S. W. Randall, and G. R. Sivakoff for helpful discussions. This work was supported by the National Aeronautics and Space Administration, primarily through the *Chandra* award GO2-3160X and through *XMM-Newton* award NAG5-13089, but also through *Chandra* awards GO4-5133X, and GO5-6126X, and through *XMM-Newton* awards NNG04GO80G, and NNG06GD54G. ELB was supported by a Clare Boothe Luce Professorship and by NASA through *Chandra* awards GO5-6137X and GO4-5148. THR acknowledges support by the Deutsche Forschungsgemeinschaft through Emmy Noether Research Grant RE 1462 and by the German BMBF through the Verbundforschung under grant no. 50 OR 0601.

## APPENDIX

### DENSITY DEPROJECTION

We basically followed Kriss et al. (1983) to deproject the gas distributions from surface brightness profile. The procedure is briefly outlined here.

Assuming spherical symmetric gas distribution, the observed X-ray surface brightness (in  $\text{ergs cm}^{-2} \text{sec}^{-1} \text{Hz}^{-1} \text{sr}^{-1}$ ) at an angle  $\theta$  (corresponding to a projected physical radius  $b$ ) from the center of the cluster is:

$$I_{\nu}^{\text{obs}}(\theta) = \frac{1}{4\pi(1+z)^3} \int_{b^2}^{\infty} \frac{\epsilon_{\nu'}(r) dr^2}{(r^2 - b^2)^{1/2}}, \quad (\text{A1})$$

where  $\epsilon_{\nu}$  is the X-ray emissivity of the gas integrated over all angles,  $\nu$  is the observed frequency,  $\nu' = (1+z)\nu$  is the emitted frequency,  $z$  is the redshift, and  $r$  is the physical distance from the cluster center.

We divided the image into  $n$  annuli bounded by the angular radii  $\theta_0 < \theta_1 < \dots < \theta_i < \theta_{i+1} < \dots < \theta_n$  and centered on the peak of the cluster emission. In this paper, we take  $\theta_0 = 0$ . Noting that  $b = \theta d_A$ , where  $d_A$  is the angular diameter distance, the flux from the annulus from  $\theta_i \rightarrow \theta_{i+1}$  is given by:

$$F_{\nu}^{\text{obs}}(\theta_i \rightarrow \theta_{i+1}) = \int_{\theta_i}^{\theta_{i+1}} I_{\nu}^{\text{obs}}(\theta) 2\pi \theta d\theta = \frac{\pi}{d_A^2} \int_{b_i^2}^{b_{i+1}^2} I_{\nu}^{\text{obs}}(b) db^2. \quad (\text{A2})$$

Putting equation (A1) into (A2), discretizing the integrals into summations, and assuming a constant emissivity ( $\epsilon_{\nu',j}$ ) within each radius ( $b_j \rightarrow b_{j+1}$ ), the observed flux can be expressed as:

$$F_{\nu}^{\text{obs}}(\theta_i \rightarrow \theta_{i+1}) = \frac{1}{3(1+z)^3 d_A^2} \left\{ \epsilon_{\nu',i} (b_{i+1}^2 - b_i^2)^{3/2} + \sum_{j=i+1}^{n-1} \epsilon_{\nu',j} [(b_{j+1}^2 - b_i^2)^{3/2} - (b_j^2 - b_i^2)^{3/2}] - (b_{j+1}^2 - b_{i+1}^2)^{3/2} + (b_j^2 - b_{i+1}^2)^{3/2} \right\}, \quad (\text{A3})$$

or in matrix form:

$$F_{\nu}^{\text{obs}}(\theta_i \rightarrow \theta_{i+1}) = \sum_{j=0}^{n-1} A_{ij} \epsilon_{\nu',j}, \quad (\text{A4})$$

where  $A_{ij}$  contains the geometrical factors in equation (A3). The matrix  $A_{ij}$  is triangular, and equation (A4) can easily be inverted to give the emissivities at each radius. Once the emissivity is known, it can then be converted to

the electron density,  $n_e$ , by the relation:

$$\epsilon_\nu = n_e^2 \Lambda_\nu, \quad (\text{A5})$$

where  $\Lambda_\nu$  is the emissivity function which depends on the temperature and the abundances. Note that  $\Lambda_\nu$  can be derived from the models used to fit the X-ray spectra.

#### COOLING TIME ESTIMATION

The cooling time of a region can be estimated from the normalization of the MEKAL model fitted by XSPEC, together with the fitted temperature, the bolometric luminosity estimated by XSPEC, and the deprojected density. The normalization of the MEKAL model in XSPEC is given by:

$$K = \frac{10^{-14}}{4\pi d_A^2 (1+z)^2} \int n_H n_e dV \text{ cm}^{-5}, \quad (\text{B1})$$

where  $d_A$  and  $z$  are the angular diameter distance and the redshift to the source, respectively,  $n_e$  and  $n_H$  are the electron and hydrogen densities, respectively, and  $V$  is the volume of the region. It is easy to show that the enthalpy  $H$  of the region is:

$$\begin{aligned} H &= \frac{5}{2} PV \\ &\approx \frac{2.5 \times 2.33 \times 4\pi d_A^2 (1+z)^2 10^{14} K}{n_e} kT \text{ ergs}. \end{aligned} \quad (\text{B2})$$

The instantaneous isobaric cooling time is then given by:

$$t_{\text{cool}}^* = \frac{H}{L_{\text{bol}}}, \quad (\text{B3})$$

where  $L_{\text{bol}}$  is the bolometric luminosity of the region which is given by XSPEC. The bolometric luminosity can be written as  $L_{\text{bol}} = \Lambda(T) n_e^2 V$ , where the emissivity function  $\Lambda(T)$  depends on the abundances and is taken from the same XSPEC model which best fits the spectrum. Then, the integrated cooling time is

$$t_{\text{cool}} = t_{\text{cool}}^* \frac{\Lambda(T)}{T^2} \int_0^T \frac{T' dT'}{\Lambda(T')} \approx \frac{t_{\text{cool}}^*}{2}. \quad (\text{B4})$$

#### REFERENCES

- Abell, G. O., Corwin, Jr., H. G., & Olowin, R. P. 1989, *ApJS*, 70, 1
- Allen, S. W., Schmidt, R. W., & Fabian, A. C. 2002, *MNRAS*, 334, L11
- Arnaud, M., et al. 2002, *A&A*, 390, 27
- Arnaud, M., Neumann, D. M., Aghanim, N., Gastaud, R., Majerowicz, S., & Hughes, J. P. 2001, *A&A*, 365, L80
- Batuski, D. J., & Burns, J. O. 1985a, *ApJ*, 299, 5
- . 1985b, *AJ*, 90, 1413
- Blanton, E. L., Sarazin, C. L., McNamara, B. R., & Wise, M. W. 2001, *ApJ*, 558, L15
- Blasi, P., Gabici, S., & Brunetti, G. 2007, *International Journal of Modern Physics A*, 22, 681
- Brunetti, G. 2004, *Journal of Korean Astronomical Society*, 37, 493
- Chen, Y., Reiprich, T. H., Böhringer, H., Ikebe, Y., & Zhang, Y.-Y. 2007, *A&A*, 466, 805
- Churazov, E., Brügggen, M., Kaiser, C. R., Böhringer, H., & Forman, W. 2001, *ApJ*, 554, 261
- Clarke, T. E., Sarazin, C. L., Blanton, E. L., Neumann, D. M., & Kassim, N. E. 2005, *ApJ*, 625, 748
- David, L. P., Jones, C., & Forman, W. 1995, *ApJ*, 445, 578
- Dickey, J. M., & Lockman, F. J. 1990, *ARA&A*, 28, 215
- Einasto, M., Einasto, J., Tago, E., Müller, V., & Andernach, H. 2001, *AJ*, 122, 2222
- Ettori, S., & Fabian, A. C. 1999, *MNRAS*, 305, 834
- Fabian, A. C. 1994, *ARA&A*, 32, 277
- Fabian, A. C., et al. 2000, *MNRAS*, 318, L65
- Falco, E. E., et al. 1999, *PASP*, 111, 438
- Feretti, L., & Giovannini, G. 1996, in *IAU Symp.* 175: Extragalactic Radio Sources, ed. R. D. Ekers, C. Fanti, & L. Padrielli, 333
- Feretti, L., & Giovannini, G. 2007, preprint (astro-ph/0703494)
- Fujita, Y., Sarazin, C. L., Kempner, J. C., Rudnick, L., Slee, O. B., Roy, A. L., Andernach, H., & Ehle, M. 2002, *ApJ*, 575, 764
- Fujita, Y., Sarazin, C. L., Reiprich, T. H., Andernach, H., Ehle, M., Murgia, M., Rudnick, L., & Slee, O. B. 2004, *ApJ*, 616, 157
- Giovanelli, R., & Haynes, M. P. 1993, *AJ*, 105, 1271
- Gitti, M., Brunetti, G., Feretti, L., & Setti, G. 2004, *A&A*, 417, 1
- Gitti, M., Feretti, L., & Schindler, S. 2006, *A&A*, 448, 853
- Heinz, S., Brügggen, M., Young, A., & Levesque, E. 2006, *MNRAS*, 373, L65
- Huchra, J. P., Vogeley, M. S., & Geller, M. J. 1999, *ApJS*, 121, 287
- Karachentsev, I. D., & Kopylov, A. I. 1981, *Soviet Astronomy Letters*, 7, 285
- Kriss, G. A., Cioffi, D. F., & Canizares, C. R. 1983, *ApJ*, 272, 439
- Lumb, D. H., Warwick, R. S., Page, M., & De Luca, A. 2002, *A&A*, 389, 93
- Markevitch, M. 2002, preprint (astro-ph/0205333)
- Markevitch, M., Forman, W. R., Sarazin, C. L., & Vikhlinin, A. 1998, *ApJ*, 503, 77
- Markevitch, M., et al. 2003, *ApJ*, 583, 70
- Marković, T., Owen, F. N., & Eilek, J. A. 2004, in *The Riddle of Cooling Flows in Galaxies and Clusters of Galaxies*, ed. T. Reiprich, J. Kempner, & N. Soker (Charlottesville: University of Virginia), 61
- McNamara, B. R., et al. 2001, *ApJ*, 562, L149
- Mohr, J. J., Geller, M. J., & Wegner, G. 1996, *AJ*, 112, 1816
- Mohr, J. J., & Wegner, G. 1997, *AJ*, 114, 25
- Peterson, J. R., & Fabian, A. C. 2006, *Phys. Rep.*, 427, 1
- Peterson, J. R., Kahn, S. M., Paerels, F. B. S., Kaastra, J. S., Tamura, T., Bleeker, J. A. M., Ferrigno, C., & Jernigan, J. G. 2003, *ApJ*, 590, 207
- Peterson, J. R., et al. 2001, *A&A*, 365, L104
- Pfommer, C., & Enßlin, T. A. 2004, *A&A*, 413, 17



- Ponman, T. J., Sanderson, A. J. R., & Finoguenov, A. 2003, MNRAS, 343, 331
- Rizza, E., Loken, C., Bliton, M., Roettiger, K., Burns, J. O., & Owen, F. N. 2000, AJ, 119, 21
- Robinson, K., et al. 2004, ApJ, 601, 621
- Sarazin, C. L. 1986, Reviews of Modern Physics, 58, 1
- Snowden, S. L., et al. 1997, ApJ, 485, 125
- Spitzer, L. 1962, Physics of Fully Ionized Gases (2nd ed.; New York: Interscience), 144
- Takizawa, M., Sarazin, C. L., Blanton, E. L., & Taylor, G. B. 2003, ApJ, 595, 142
- Vernaleo, J. C., & Reynolds, C. S. 2006, ApJ, 645, 83
- Voit, G. M., & Donahue, M. 2005, ApJ, 634, 955
- White, D. A., Jones, C., & Forman, W. 1997, MNRAS, 292, 419
- Xue, Y.-J., & Wu, X.-P. 2000, MNRAS, 318, 715
- Zucca, E., Zamorani, G., Scaramella, R., & Vettolani, G. 1993, ApJ, 407, 470

TABLE 1  
*XMM-Newton* X-RAY POINT SOURCES WITH NED IDENTIFICATIONS

X-ray RA	X-ray Dec	NED object	Type <sup>a</sup>	NED RA	NED Dec	Redshift	Separation <sup>b</sup>
23:36:04.8	+21:06:11.2	2MASX J23360455+2106127	G/IrS	23:36:04.6	+21:06:13	0.066130	3''
23:36:09.6	+21:20:25.1	MG3 J233615+2120	RadioS	23:36:09.7	+21:20:25	...	1''
23:36:15.8	+21:06:11.5	Abell 2626:[SPS89] 08	VisS/RadioS	23:36:16.2	+21:06:21	...	11''
23:36:24.5	+21:09:03.6	IC 5337	G/IrS/RadioS	23:36:25.1	+21:09:02	0.054988	9''
23:36:30.5	+21:08:47.0	IC 5338	G/IrS/RadioS	23:36:30.6	+21:08:50	0.054900	3''
23:36:53.8	+21:13:32.9	2MASX J23365372+2113322	G/IrS	23:36:53.7	+21:13:32	0.056100	2''
23:36:54.2	+21:15:31.7	2MASX J23365415+2115302	G/IrS	23:36:54.2	+21:15:29	0.054200	3''
23:36:57.1	+21:14:05.6	2MASX J23365722+2114032	G/IrS	23:36:57.2	+21:14:03	0.038040	3''
23:37:32.4	+21:09:07.6	2MASX J23373222+2109020	G/IrS	23:37:32.2	+21:09:02	0.184400	6''

<sup>a</sup> The source type as classified by NED: G=Galaxies; IrS=Infrared Source; RadioS=Radio Source; VisS=Visual Sources.

<sup>b</sup> Separation between the X-ray point source and source identified by NED.

TABLE 2  
*Chandra* X-RAY POINT SOURCES

RA	Dec	
23:36:15.82	+21:08:55.4	
23:36:21.31	+21:13:29.7	
23:36:21.41	+21:11:35.4	
23:36:24.61	+21:08:47.7	
23:36:24.81	+21:10:16.7	
23:36:25.04	+21:09:03.0	IC 5337
23:36:25.60	+21:13:07.7	
23:36:30.52	+21:08:47.0	IC 5338
23:36:33.30	+21:08:36.7	
23:36:36.98	+21:10:51.8	
23:36:37.46	+21:06:21.0	
23:36:38.43	+21:08:26.1	
23:36:45.60	+21:07:49.3	
23:36:46.84	+21:08:07.8	

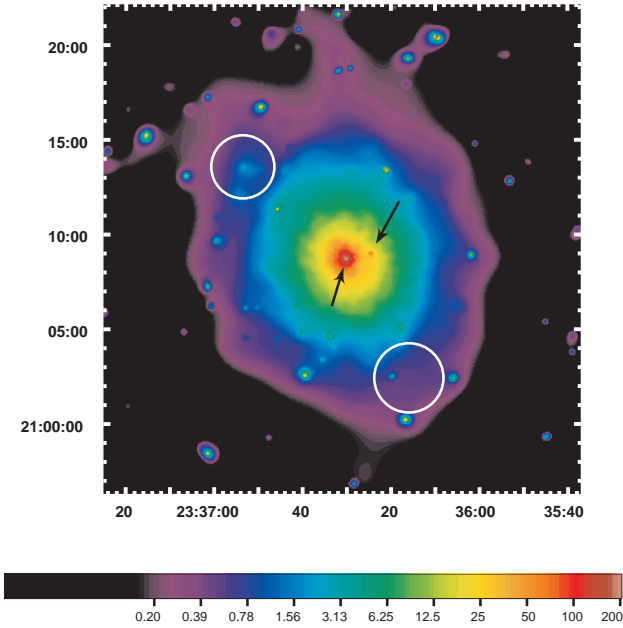


FIG. 1.— Background-subtracted, exposure-corrected, adaptively smoothed mosaic of the *XMM-Newton* EPIC MOS1 and MOS2 images in the 0.3–10 keV band. The image was smoothed to a signal-to-noise ratio of 3. The units for the color scale are counts per binned pixel, where each binned pixel has a size of  $4''.1 \times 4''.1$ . The arrows on the left and right indicate the cD galaxy IC 5338 and the S0 galaxy IC 5337, respectively. Two outer extended emission regions are indicated with white circles. It should be noted that there is a chip gap at about  $5''.5$  from the center which makes the northeast extended X-ray source appear to be more distinct than it actually is.

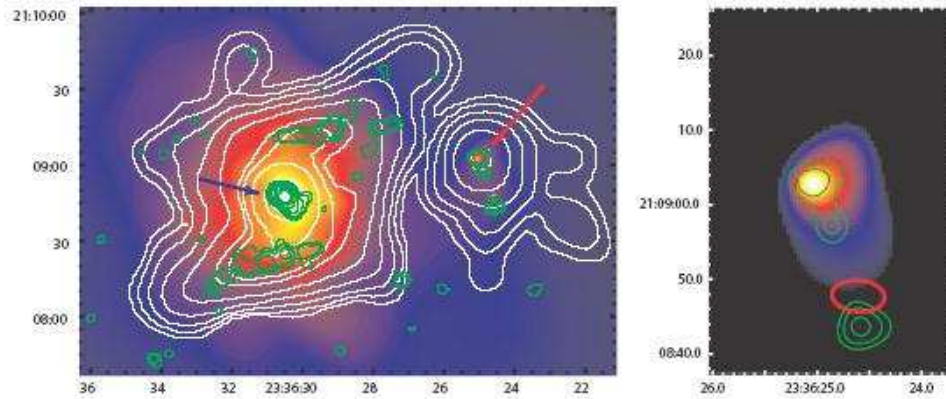


FIG. 2.— *Left panel:* Background subtracted, exposure-corrected, adaptively smoothed *Chandra* image of the central  $3''.5 \times 2''.4$  region of the cluster in the 0.3–10 keV band. The image was smoothed to a signal-to-noise ratio of 3. The *Chandra* image shows the details of the inner region of the cooling core. The white solid lines are 1.5 GHz C-array radio contours showing the mini-halo. The green solid lines are 1.5 GHz B-array radio contours showing the radio bar structures. Both radio contours were taken from Gitti et al. (2004). The arrows on the left and right indicate the cD galaxy IC 5338 and the S0 galaxy IC 5337, respectively. *Right panel:* Background subtracted, exposure-corrected, adaptively smoothed *Chandra* image centered on the S0 galaxy IC 5337. The image was smoothed to a signal-to-noise ratio of 4, with an intensity scale chosen to show the bow-shock-like shape. The southern source (red ellipse) was removed and replaced by the average surrounding X-ray intensity before adaptively smoothing. The green contours are from the VLA 1.5 GHz B-array radio image taken from Gitti et al. (2004), with the lowest contour level being a signal-to-noise ratio of 3.

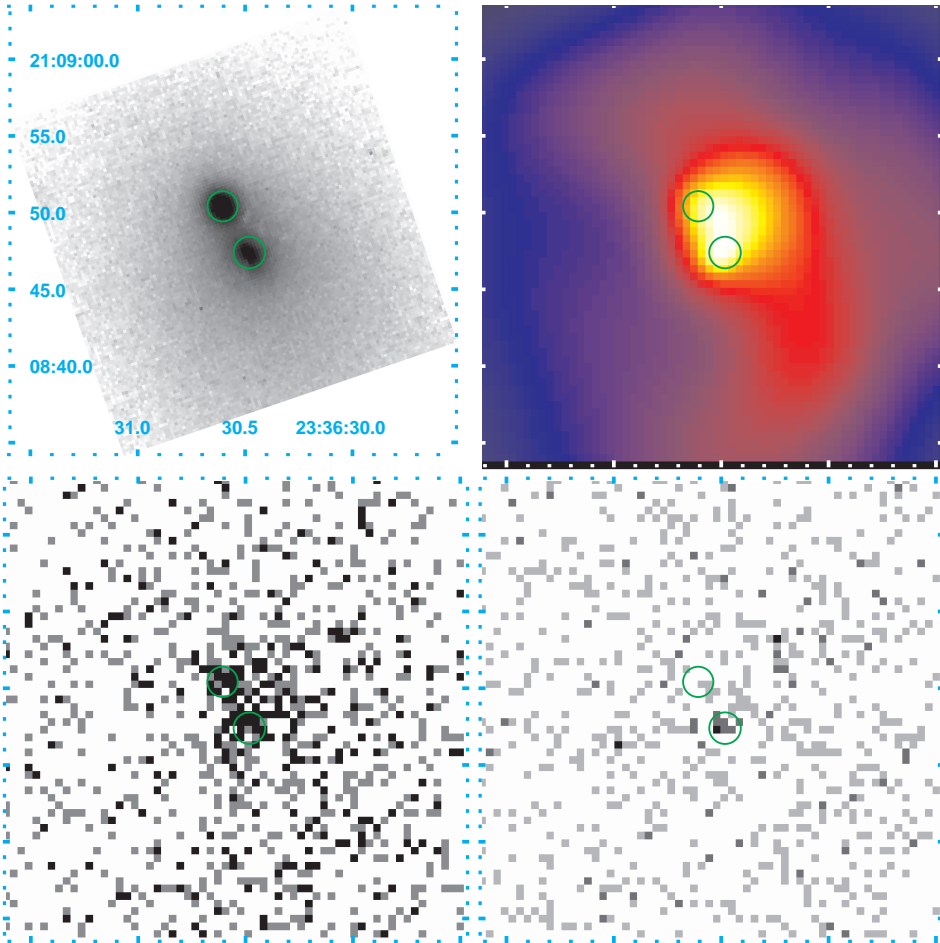


FIG. 3.— Images of the two nuclei of the cD galaxy IC 5338 in Abell 2626. All images show the same field of view of  $30'' \times 30''$ . *Upper left panel:* Optical image from *HST* archive. The image was taken with WFPC2 using the F555W filter. The two green circles, included in the other panels, are centered at the two optical nuclei observed by *HST*. *Upper right panel:* Background-subtracted, exposure-corrected, adaptively smoothed *Chandra* image in 0.3–10 keV band. The image was smoothed to a signal-to-noise ratio of 3. The color represents the X-ray intensity from high (white yellow) to low (dark blue). *Lower left panel:* Raw *Chandra* image in the soft (0.3–2 keV) band. Two intensity peaks can be identified. *Lower right panel:* Raw *Chandra* image in the hard (2–10 keV) band. Only the southwest nucleus corresponds to the peak in the hard band.

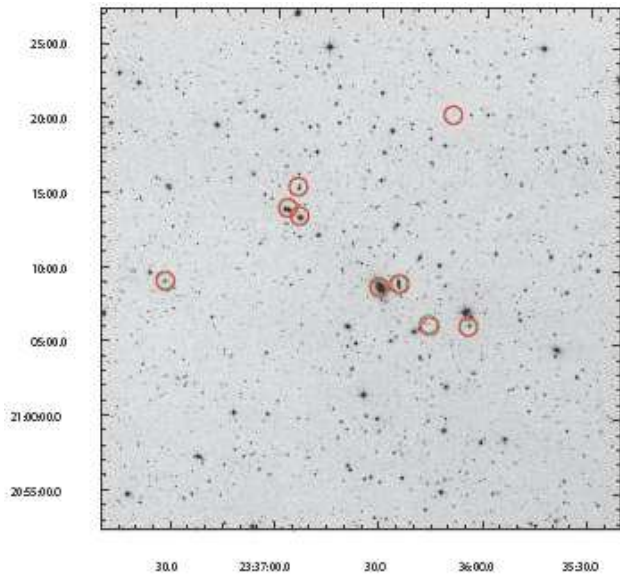


FIG. 4.— Optical image from the Digital Sky Survey showing the 9 *XMM-Newton* X-ray sources with identifications in NED (Table 1). The red circles are centered on the X-ray positions determined with *XMM-Newton*. There are green circles centered on the optical positions from NED, but they overlap so completely with the red circles that they are barely visible. NED objects are considered possible identifications if they are within  $20''$  of an X-ray source. In fact all optical counterparts identified are within  $11''$ .

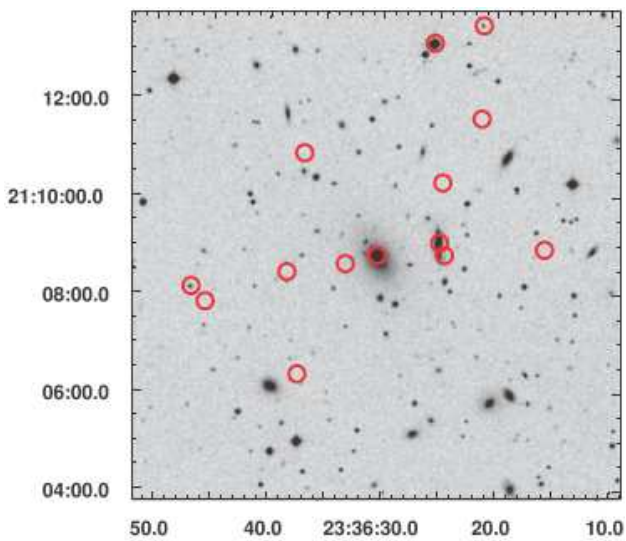


FIG. 5.— Optical image from the Digital Sky Survey showing the positions (red circles) of the 14 X-ray point sources detected with *Chandra* (Table 2).

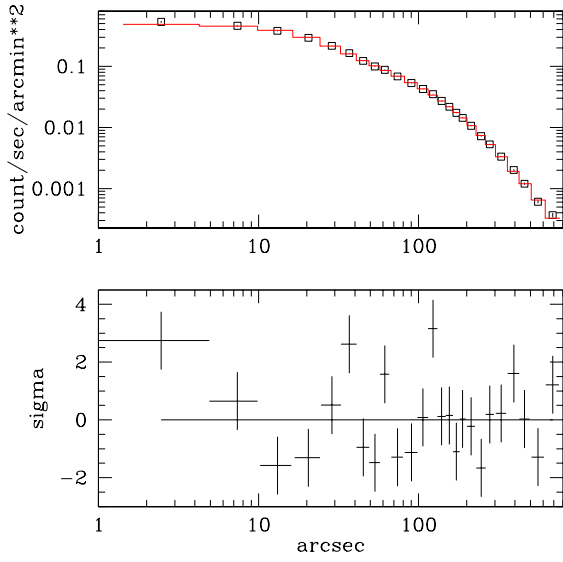


FIG. 6.— *Upper panel:* Azimuthally averaged X-ray surface brightness profile from the *XMM-Newton* MOS1 and MOS2 observations of Abell 2626. The squares are the X-ray data, while the solid line is the fit to a double  $\beta$  model. The tiny error bars within the squares on the surface brightness are too small to be easily seen. *Lower panel:* The residuals to the best fit double beta model, in unit of  $\sigma$ . The horizontal error bars show the widths of the bins used to accumulate the counts. The vertical error bars are at the  $1\sigma$  level.

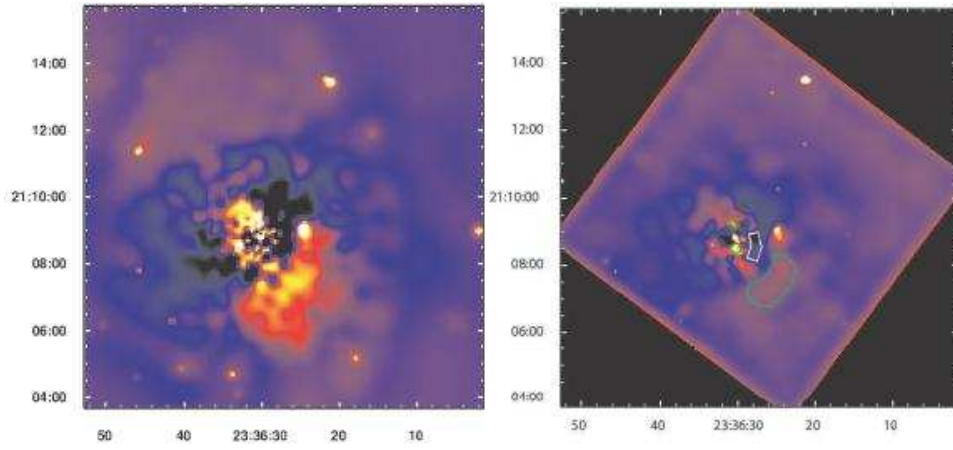


FIG. 7.— *Left panel:* Residual map from the *XMM-Newton* MOS1 and MOS2 observations of Abell 2626, generated from a background-subtracted image. Yellow represents the largest excess, while black is the greatest deficit. *Right panel:* Residual map from the *Chandra* observation of Abell 2626, generated from a background-subtracted image. Yellow represents the largest excess, while black is the greatest deficit. There is an excess coincident with the center of the central cD galaxy, which is partly surrounded by a trough of reduced X-ray surface brightness at a radius of about  $15''$ . There are two localized regions of excess south and north of the central peak, which are indicated with green circles. There is an extended deficit about  $50''$  west of the center, which is indicated with a white polygon. An extended region of excess emission is seen about  $110''$  SW of the center, which is indicated with a green polygon.

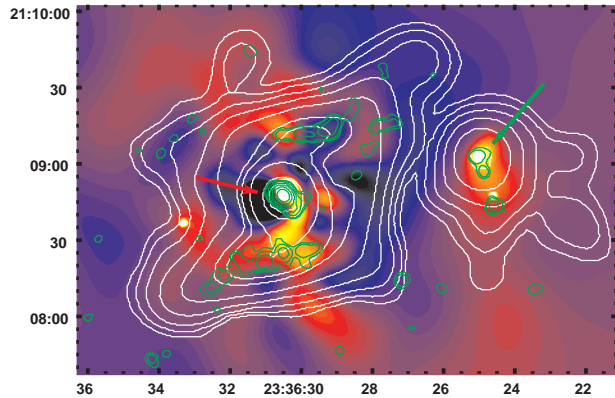


FIG. 8.— Residual map from *Chandra* observation of the central  $3'5 \times 2'4$  region of Abell 2626, generated from a background-subtracted image. The color scale from yellow to red to blue to black represents the residuals, running from excess to deficit. The white solid lines are 1.5 GHz C-array radio contours showing the mini-halo. The green solid lines are 1.5 GHz B-array radio contours showing the radio bar structures. Both radio contours were taken from Gitti et al. (2004). The arrows on the left and right indicate the cD galaxy IC 5338 and the S0 galaxy IC 5337, respectively.

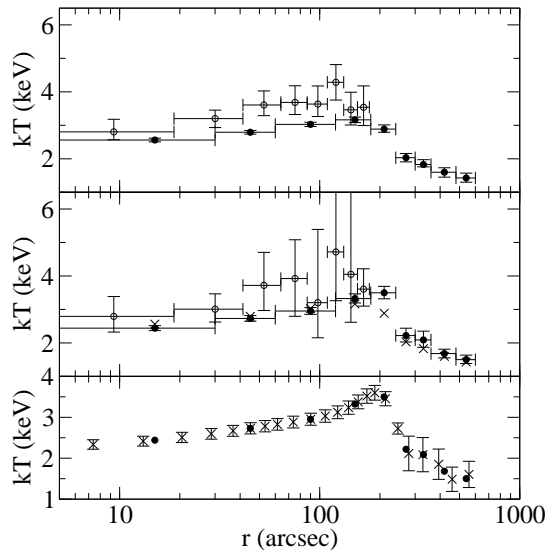


FIG. 9.— *Upper Panel:* Profile of the azimuthally averaged, projected temperature  $T$  of Abell 2626. The *XMM-Newton* (*Chandra*) data are shown as solid (open) circles. *Middle Panel:* Profile of the azimuthally averaged, deprojected temperature  $T$  of Abell 2626. The *XMM-Newton* (*Chandra*) data are shown as solid (open) circles. The black crosses are the projected temperatures from the *XMM-Newton* data in the upper panel for comparison (without error bars for clarity). In both the upper and middle panels, the error bars are at the 90% confidence level. *Lower Panel:* Crosses are the temperatures calculated from interpolation of the original *XMM-Newton* deprojected temperature profile; this interpolated profile was used for the pressure/entropy/time scales deprojection and the mass profile analysis in §§ 4.3, 4.4, & 4.5. The interpolated temperature profile for the *Chandra* data analysis is similar but not shown for clarity. The errors are assigned as 5 (20)% at radii of smaller (larger) than  $250''$  to include possible systematic errors. The solid circles are the original *XMM-Newton* measured deprojected temperatures as shown in the middle panel, without error bars for clarity.

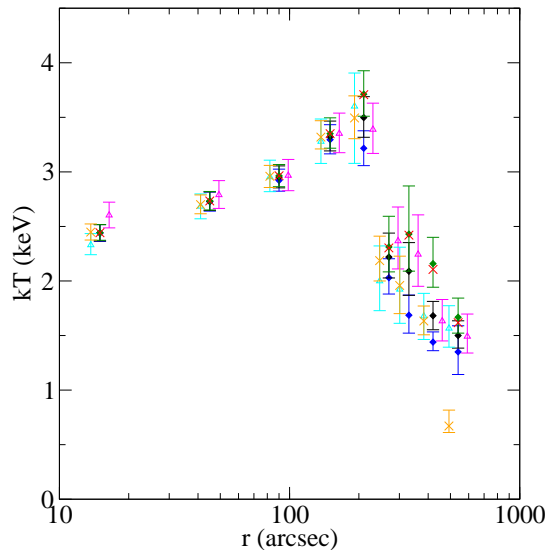


FIG. 10.— Profile of the azimuthally averaged, deprojected temperature  $T$  of Abell 2626 with different *XMM-Newton* backgrounds. The black diamonds give our adopted *XMM-Newton* temperature profile (the black solid circles in the second panel of Figure 9). The other temperature profiles are generated by: 1a) (blue diamonds) increasing the blank-sky background normalizations by 10% (20%) for MOS (PN); 1b) (green diamonds) decreasing the blank-sky background normalizations by 10% (20%) for MOS (PN); 2) (red crosses) using the blank-sky backgrounds without renormalization (no error bars for clarity); 3) (magenta triangles) using the MOS1+MOS2 spectra only (data shifted to the right for clarity); 4) (cyan triangles) using the PN spectra only (data shifted to the left for clarity); 5) (orange crosses) adding an extra 0.2 keV MEKAL component to represent variations in the soft Galactic component (normalization free and allowed to be negative in each annulus, data shifted to the left for clarity). The error bars are at the 90% confidence level.



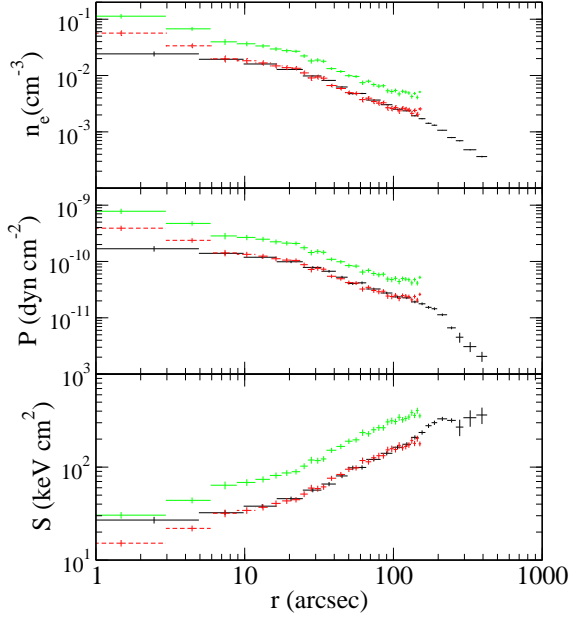


FIG. 11.— *Upper Panel:* Azimuthally averaged electron density profile of Abell 2626. The *XMM-Newton* (*Chandra*) data are shown as black solid (red dashed) symbols. For clarity, we have also multiplied the *Chandra* data and error bars by a factor of 2 (green solid symbols). The error bars are at the  $1\sigma$  level. *Middle Panel:* Azimuthally averaged pressure profile, with the same notation as the upper panel. *Lower Panel:* Azimuthally averaged entropy profile, with the same notation as the upper panel.

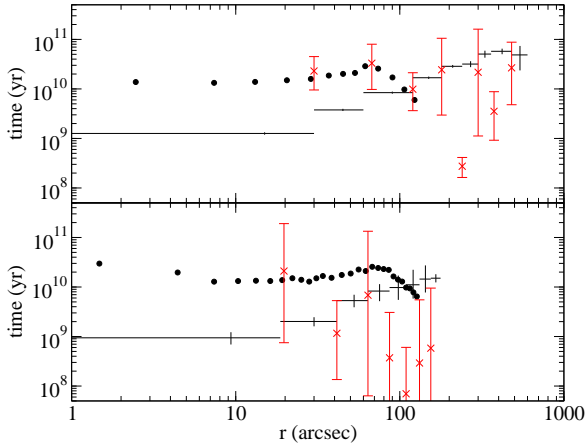


FIG. 12.— *Upper Panel:* Cooling and thermal conduction time scales in Abell 2626 obtained from the *XMM-Newton* data. The cooling times are the plus symbols with horizontal bars showing the annular regions sampled. The conduction time scales derived directly from individual data points are the crosses with larger vertical error bars. The dots are conduction time scales calculated by interpolating the temperature profile of the cluster (see text in § 4.4). The radial regions for the conduction time are not given for clarity. The error bars are at the  $1\sigma$  level. *Lower Panel:* Same as the upper panel, but with the time scales calculated from the *Chandra* data.

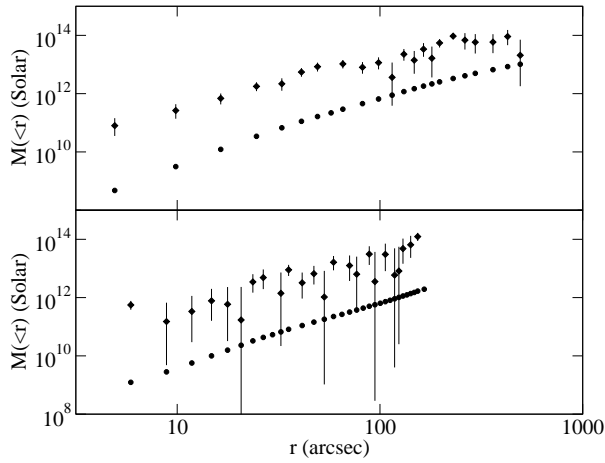


FIG. 13.— *Upper panel* is the interior mass profile [ $M(< r)$ ], of Abell 2626 obtained from *XMM-Newton* data, while the *lower panel* is from *Chandra* data. The total mass is shown with diamond symbols, while the gas mass points are circles. The error bars on the masses are calculated using propagation of errors at  $1 \sigma$  level. The error bars on the gas mass are plotted, but are smaller than the circle symbols.

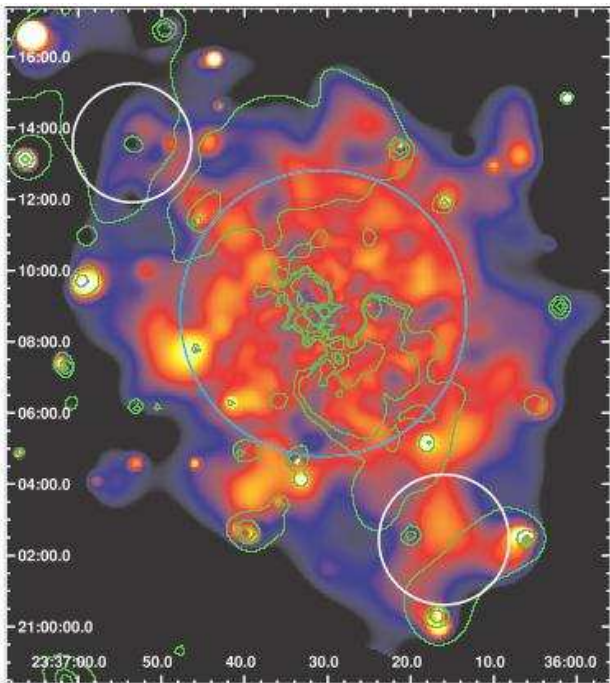


FIG. 14.— Hardness ratio ( $HR$ ) map of Abell 2626 from the *XMM-Newton* observation. Background was subtracted from the images combined to calculate the hardness ratio. The color scale ranges from black ( $HR \sim 0$ ) to blue ( $HR \sim 0.1$ ) to red ( $HR \sim 0.3$ ) to yellow ( $HR \sim 0.5$ ) to white ( $HR \sim 2.5$ ), showing increasingly hard emission. The green solid lines are contours from *XMM-Newton* residual map (left panel of Figure 7) showing positive residuals (excess emission). The white circles are the regions of extended X-ray emissions to the northeast and southwest. The cyan circle has a radius of  $240''$  corresponding to the jump in the temperature profile.

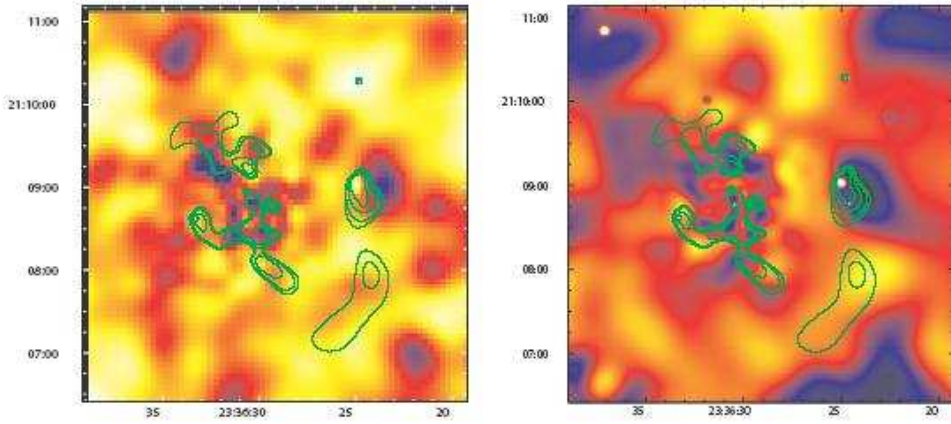


FIG. 15.— *Left panel:* Central portion ( $4'6 \times 4'7$ ) of the *XMM-Newton* hardness ratio map (Figure 14). The color scale is similar to that in Figure 14, but with the hardness ratio extremes being  $\sim 0.2$  and  $0.35$  (dark blue to white yellow). The green solid lines are contours from the *Chandra* residual map (right panel of Figure 7) showing the excess emission. *Right panel:* Hardness ratio map from the *Chandra* data, for the same regions and with the same contours as the left panel. Background was subtracted from the images combined to calculate the hardness ratio. The color scale is similar to that in Figure 14, but with the hardness ratios in the range from  $\sim 0.1$  to  $1.5$  (dark blue to white yellow). The cD galaxy IC 5338 and the S0 galaxy IC 5337 are located at  $(23:36:31, +21:08:47)$  and  $(23:36:25, +21:09:03)$ , respectively.

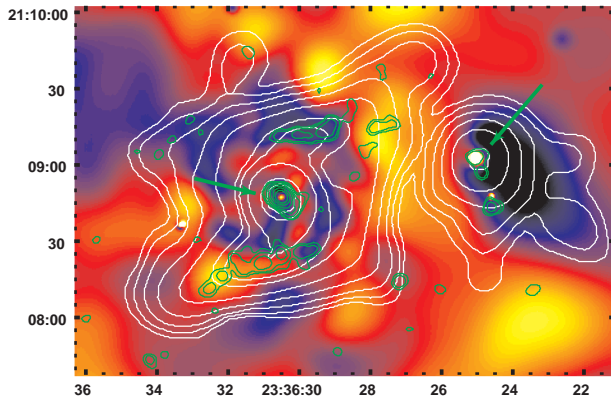


FIG. 16.— Central region ( $3'5 \times 2'4$ ) of the hardness ratio map from the *Chandra* observation. Background was subtracted from the images combined to calculate the hardness ratio. The color scale is roughly the same as in the right panel of Figure 15. The white solid lines are 1.5 GHz C-array radio contours showing the mini-halo. The green solid lines are 1.5 GHz B-array radio contours showing the radio bar structures. Both radio contours were taken from Gitti et al. (2004). The arrows on the left and right indicate the cD galaxy IC 5338 and the S0 galaxy IC 5337, respectively.